

# Glyoxal tropospheric column retrievals from TROPOMI, multi-satellite intercomparison and ground-based validation

Christophe Lerot<sup>1</sup>, François Hendrick<sup>1</sup>, Michel Van Roozendael<sup>1</sup>, Leonardo M.A. Alvarado<sup>2,3</sup>, Andreas Richter<sup>3</sup>, Isabelle De Smedt<sup>1</sup>, Nicolas Theys<sup>1</sup>, Jonas Vlietinck<sup>1</sup>, Huan Yu<sup>1</sup>, Jeroen Van Gent<sup>1</sup>, Trissevgeni Stavrakou<sup>1</sup>, Jean-François Müller<sup>1</sup>, Pieter Valks<sup>4</sup>, Diego Loyola<sup>4</sup>, Hitoshi Irie<sup>5</sup>, Vinod Kumar<sup>6</sup>, Thomas Wagner<sup>6</sup>, Stefan F. Schreier<sup>7</sup>, Vinayak Sinha<sup>8</sup>, Ting Wang<sup>9</sup>, Pucai Wang<sup>9</sup>, Christian Retscher<sup>10</sup>

<sup>1</sup> Royal Belgian Institute for Space Aeronomy (BIRA-IASB), Brussels, Belgium

<sup>2</sup> Alfred Wegner Institute, Helmholtz Center for Polar and Marine Research, Bremerhaven, Germany

<sup>3</sup> University of Bremen, Institute of Environmental Physics, Bremen, Germany

<sup>4</sup> Institut für Methodik der Fernerkundung (IMF), Deutsches Zentrum für Luft und Raumfahrt (DLR), Oberpfaffenhofen, Germany

<sup>5</sup> Center for Environmental Remote Sensing, Chiba University, Japan

<sup>6</sup> Max Planck Institute for Chemistry (MPIC), Mainz, Germany

<sup>7</sup> Institute of Meteorology and Climatology, University of Natural Resources and Life Sciences, Vienna, Austria

<sup>8</sup> Indian Institute of Science Education and Research Mohali, Mohali, India

<sup>9</sup> Institute of Atmospheric Physics, Chinese Academy of Sciences (CAS), Beijing, China

<sup>10</sup> European Space Agency, ESRIN, Frascati, Italy

*Correspondence to:* Christophe Lerot, [Christophe.Lerot@aeronomie.be](mailto:Christophe.Lerot@aeronomie.be)

**Abstract.** We present the first global glyoxal (CHOCHO) tropospheric column product derived from the Tropospheric Monitoring Instrument (TROPOMI) on board of the Sentinel-5 Precursor satellite. Atmospheric glyoxal results from the oxidation of other non-methane volatile organic compounds (NMVOCs) and from direct emissions caused by combustion processes. Therefore, this product is a useful indicator of VOC emissions. It is generated with an improved version of the BIRA-IASB scientific retrieval algorithm relying on the Differential Optical Absorption Spectroscopy (DOAS) approach. Among the algorithmic updates, the DOAS fit now includes corrections to mitigate the impact of spectral misfits caused by scene brightness inhomogeneity and strong NO<sub>2</sub> absorption. The product comes along with a full error characterization, which allows providing random and systematic error estimates for every observation. Systematic errors are typically in the range of 1-3x10<sup>14</sup> molec/cm<sup>2</sup> (~30-70% in emission regimes). Random errors are larger (>6x10<sup>14</sup> molec/cm<sup>2</sup>) but can be reduced by averaging observations in space and/or time. Benefiting from a high signal-to-noise ratio and a large number of small-size observations, TROPOMI provides glyoxal tropospheric column fields with an unprecedented level of details.

Using the same retrieval algorithmic baseline, glyoxal column data sets are also generated from the Ozone Monitoring Instrument (OMI) on Aura and from the Global Ozone Monitoring Experiment-2 (GOME-2) on board of Metop-A and Metop-B. Those four data sets are intercompared over large-scale regions worldwide and show a high level of consistency. The satellite glyoxal columns are also compared to glyoxal columns retrieved from ground-based Multi-Axis (MAX-) DOAS instruments at nine stations in Asia and Europe. In general, the satellite and MAX-DOAS instruments provide consistent glyoxal columns both in terms of absolute values and variability. Correlation coefficients between TROPOMI and MAX-DOAS glyoxal columns range between 0.61 and 0.87.

The correlation is only poorer at one mid-latitude station, where satellite data appears low biased during wintertime. The mean absolute glyoxal columns from satellite and MAX-DOAS generally agree well for low/moderate columns with differences less than  $1 \times 10^{14}$  molec/cm<sup>2</sup>. A larger bias is identified at two sites where the MAX-DOAS columns are very large. Despite this systematic bias, the consistency of the satellite and MAX-DOAS glyoxal seasonal variability is excellent.

## 1. Introduction

Exposure to poor air quality kills millions of people annually (e.g. Vohra et al., 2021; World Health Organization, 2016) due to natural and human emissions of a large range of particulate matters and gases, including among others nitrous oxides (NO<sub>x</sub>), sulphur dioxide, carbon monoxide, methane and volatile organic compounds (VOCs). The latter, in combination with NO<sub>x</sub>, play a significant role in the secondary production of tropospheric ozone (Jacob, 2000), which is highly toxic for the respiratory system and also contributes to global warming because of its absorption in the thermal infrared. Global measurements of atmospheric concentrations of the ozone precursors are therefore crucial. The number of VOCs that can be found in the atmosphere is manifold, but only a few of them can be probed using remote sensing techniques. For example, formaldehyde (HCHO) measurements have been used in many studies as a proxy for probing emissions of non-methane VOCs of biogenic, pyrogenic and anthropogenic origin (e.g. Abbot et al., 2003; Barkley et al., 2013; Bauwens et al., 2016; Beekmann and Vautard, 2010; Curci et al., 2010; Jin et al., 2020; Marais et al., 2012; Palmer et al., 2006; Stavrou et al., 2016; Wells et al., 2020).

With a lifetime of a few hours, glyoxal (CHOCHO) is another short-lived VOC that can be detected remotely, offering the potential to provide information on Non-Methane VOC (NMVOC) emissions. Over the past few years, an increasing number of studies (e.g. Cao et al., 2018; Chan Miller et al., 2017; Fu et al., 2008; Li et al., 2016; Liu et al., 2012; Stavrou et al., 2009, 2016; Wittrock et al., 2006) have exploited glyoxal measurements from space, often in combination with formaldehyde. Being produced from similar sources, those two species are complementary as they have different production yields. For example, the oxidation of aromatics produces glyoxal with a much higher yield than formaldehyde (Cao et al., 2018). Although being both mostly produced via the oxidation of other VOCs, direct emissions from anthropogenic and fire activities also occur, and contribute more to the glyoxal global budget than to the formaldehyde one (Stavrou et al., 2009b, 2009a). This motivated many studies to investigate the ratio of glyoxal to formaldehyde concentrations or columns as a possible metric to discriminate between different types of VOC emissions (e.g. Chan Miller et al., 2014; DiGangi et al., 2012; Hoque et al., 2018; Kaiser et al., 2015; Vrekoussis et al., 2010). Glyoxal measurements are also essential for establishing the global budget of secondary organic aerosols (SOAs). Indeed, with a high solubility in water, glyoxal undergoes heterogeneous uptake on aerosols and cloud droplets where the subsequent aqueous-phase chemistry forms SOA (Chan et al., 2010; Fu et al., 2008; Hallquist et al., 2009; Knote et al., 2014; Li et al., 2016; Volkamer et al., 2007).

Glyoxal has three absorption bands in the visible spectral range that have been exploited to remotely retrieve information on its atmospheric abundance using the Differential Optical Absorption Spectroscopy method (DOAS, Platt and Stutz, 2008) applied to ground-based (e.g. Benavent et al., 2019; Hoque et al., 2018; Javed et al., 2019; Schreier et al., 2020), air-borne (e.g. Kluge et al., 2020; Volkamer et al., 2015), ship-borne (e.g. Behrens et al., 2019; Sinreich et al., 2010) and space-based instruments. The first global glyoxal tropospheric column

observations from space have been realized by Wittrock et al. (2006) using nadir measurements from the SCIAMACHY (SCanning Imaging Absorption spectroMeter for Atmospheric CartographY) instrument. Based on this pioneering work, different glyoxal data products were derived from the Global Ozone Monitoring Experiment-2 (GOME-2) (Lerot et al., 2010; Vrekoussis et al., 2009) and from the Ozone Monitoring Instrument (OMI) (Alvarado et al., 2014; Chan Miller et al., 2014). All those different products rely on a similar DOAS approach, but generally differ from each other by the choice of the fit settings and of the auxiliary input data.

In general, the glyoxal optical depth is very low ( $< 5 \times 10^{-4}$ ), typically one order of magnitude smaller than the  $\text{NO}_2$  optical depth in the same spectral range. This results in retrievals prone-to-noise, requiring to average many of them to extract meaningful glyoxal signals. With an enhanced spatial resolution resulting in a number of observations more than ten times larger than provided by its predecessor OMI, the TROPOspheric Monitoring Instrument (TROPOMI), operating since 2017, allows observing weak atmospheric absorbers with an unprecedented level of spatio-temporal details. This has been illustrated by Alvarado et al. (2020a) who investigated the large amounts of formaldehyde and glyoxal emitted by the intense North-American wildfires in August 2018 as observed by TROPOMI for several days and over long distances. Theys et al. (2020) have evaluated the respective contributions to the hydroxyl radical production in fresh fire plumes from nitrous acid, VOCs and other sources with the support of different TROPOMI data sets, including the glyoxal data product described here.

This work presents the latest version of the BIRA-IASB scientific glyoxal tropospheric column retrieval algorithm that has been applied to three years of TROPOMI measurements, and also to data from the predecessor nadir instruments OMI and GOME-2A/B. The quality of the TROPOMI glyoxal retrievals is investigated with (1) a global intercomparison of the satellite glyoxal data products generated with a common algorithm and (2) comparisons with independent glyoxal measurements from a series of Multi-AXis DOAS (MAX-DOAS) instruments located at nine stations in Asia and Europe.

After a brief introduction of the satellite instruments used in this study in Section 2, the retrieval algorithm and its different steps are described in Section 3, with emphasis on the updated and innovative aspects compared to heritage studies. This section also presents the typical random and systematic errors associated to the retrievals and how they are estimated for each individual measurement. Section 4 presents the evaluation of the inter-satellite consistency by comparing both seasonal global spatial patterns as seen from different instruments as well as monthly mean time series and seasonal cycles in a series of selected large-scale regions. Finally, Section 5 presents validation results based on MAX-DOAS data.

## **2. TROPOMI and other nadir-viewing satellite sensors**

TROPOMI was launched on 13 October 2017 on board of the Sentinel-5 precursor platform. It flies on a sun-synchronous Low Earth Orbit (LEO) with an ascending node crossing the equator at the local time of 13:30. In the series of Sentinel missions from the European Union Copernicus programme, it is the first one dedicated to atmospheric composition. The instrument operates in a nadir viewing mode and measures Earthshine radiances and solar irradiances in the ultraviolet (UV), visible, near infrared and short infrared spectral bands. It aims at providing column amounts of a number of key pollutants, such as ozone ( $\text{O}_3$ ),  $\text{NO}_2$ ,  $\text{SO}_2$ ,  $\text{HCHO}$ ,  $\text{CO}$ ,  $\text{CH}_4$  as well as cloud and aerosol parameters. TROPOMI offers a quasi-daily global coverage at the unprecedented spatial

resolution of  $3.5 \times 5.5 \text{ km}^2$  ( $3.5 \times 7 \text{ km}^2$  before August 2019) in the UV-visible spectral range. It is an imager-type instrument using a two-dimensional Charge Coupled Device (CCD) for the light measurements, the detector columns being used for the spectral resolution while the rows are binned to resolve spatially the 2600 km across-track swath into 450 individual ground pixels. The spectral resolution of the instrument is about 0.5 nm and offers a remarkably high signal-to-noise ratio of about 1500 in band 4 (405-500 nm) used in this study. More details on the instrument and its performance can be found in (Kleipool et al., 2018; Ludewig et al., 2020; Schenkeveld et al., 2017; Veefkind et al., 2012). The TROPOMI measurements allow to derive the vertical columns of multiple species, some of them not included among the operational products listed above. Glyoxal is one of them and the details on how its column quantities are retrieved will be described in the next section.

The TROPOMI design strongly inherits from past nadir-viewing sensors, and in particular from the Ozone Monitoring Instrument (OMI) that we use to evaluate the TROPOMI glyoxal product presented in this work. OMI (Levelt et al., 2006) is also an imager instrument and flies on an early afternoon orbit since October 2004. The OMI swath, divided into 60 across-track pixels with a size varying from  $13 \times 24 \text{ km}^2$  (at nadir) to  $13 \times 150 \text{ km}^2$  (at the edges), allowed a daily global coverage before being limited in 2008 by the so-called row anomaly. The latter consists in a modification of the signal recorded by OMI at specific rows, due to a mechanical obstruction of the field of view, and leads to lower quality spectral measurements (Torres et al., 2018). We also exploit spectral measurements from the Global Ozone Monitoring Experiment-2 (GOME-2) instruments aboard the Metop-A and Metop-B platforms. In contrast to OMI and TROPOMI, the GOME-2 instruments (Munro et al., 2016) fly on early morning LEOs with local equator crossing times around 09:30 and are scanning spectrometers, meaning that across-track pixels are successively sounded. The scan is divided into 24 pixels for a total swath of 1920 km, providing global coverage in 1.5 day. Each pixel has a size of  $80 \times 40 \text{ km}^2$ . After the launch of Metop-B, the GOME-2A swath was reduced to 960 km in July 2013, leading to ground pixel two times smaller.

### 3. Description of the Algorithm

The algorithm for retrieving tropospheric vertical columns of glyoxal relies on a classical DOAS approach (Platt and Stutz, 2008). This approach consists first in fitting measured optical depths in an optimized spectral window to derive the so-called slant column densities *SCDs* (atmospheric concentration integrated along the effective light path) of the absorbers. The latter are thereafter converted into vertical column densities *VCDs* (concentration vertically integrated from the satellite ground pixel up to the top of the atmosphere) with air mass factors (*AMFs*) obtained by modelling the radiative transfer through the atmosphere. An additional background correction procedure is often applied for weak absorbers such as glyoxal in order to reduce as much as possible the presence of systematic biases caused by spectral interferences.

The glyoxal algorithm presented here largely inherits from past developments for predecessor nadir-viewing satellite sensors (Alvarado et al., 2014, 2020; Chan Miller et al., 2014; Lerot et al., 2010; Vrekoussis et al., 2009; Wittrock et al., 2006). ~~In the following subsections, we further describe each algorithmic component, with emphasis on its specificities.~~ Figure 1 illustrates for one day of TROPOMI data the resulting main output of every ~~algorithmic components, which we further describe in the following sections, with emphasis on their specificities.~~ The retrievals are provided with estimates for the random and systematic errors, which are discussed in subsection 3.4.

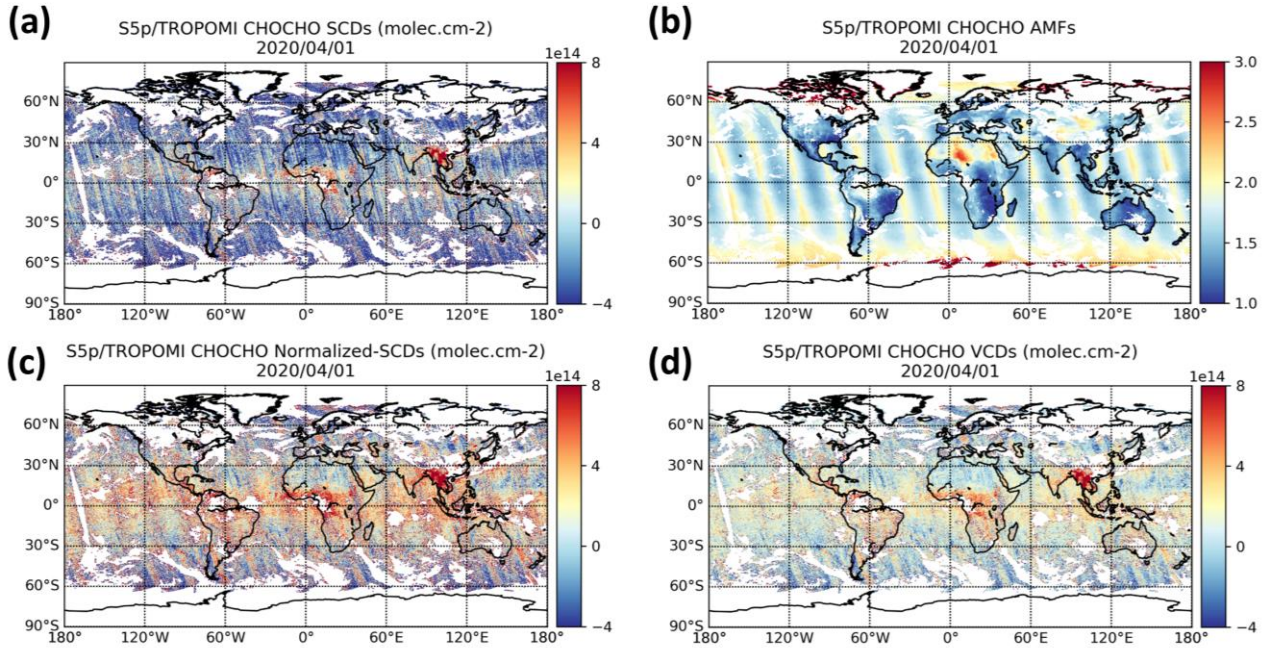


**Figure 1: Illustration of the different glyoxal algorithmic steps for one day of TROPOMI data (01/04/2020). (a) Glyoxal SCDs retrieved from the DOAS spectral fits; (b) Glyoxal AMFs; (c) Glyoxal normalized-SCDs resulting from the background correction procedure; (d) Final retrieved glyoxal VCDs. The data has been gridded at the spatial resolution of 0.25°.**

### 3.1. DOAS fit

To exploit the glyoxal absorption bands, we use a fitting window from 435 to 460 nm encompassing the two most intense bands, which has shown in the past to provide reliable results (Barkley et al., 2017; Lerot et al., 2010). This has been confirmed by sensitivity tests carried out by Alvarado et al. (2014) and Chan Miller et al. (2014). Owing to its low optical depth ( $<5 \times 10^{-4}$ ), any poorly fitted feature in the radiance measurements may affect the retrieved glyoxal SCD. It is therefore crucial to account for any physical or instrumental effect in order to optimise the fit quality as much as possible. Different aspects of the algorithm contribute to achieve this.

The wavelength grids of the measured spectra are recalibrated before the actual DOAS fits with a cross-correlation procedure (Danckaert et al., 2017; De Smedt et al., 2018) during which the position of the lines in the measured irradiance spectrum is fitted to an external solar atlas (Chance and Kurucz, 2010), convolved to the satellite spectral resolution. This recalibration procedure is done once per orbit and separately for every detector row of the instrument.

Although the DOAS fit generally uses an irradiance as the reference spectrum, it is common practice, in the case of weak tropospheric absorbers, to replace it by a mean radiance spectrum recorded in a remote region where the concentration of the gas of interest is low (e.g. De Smedt et al., 2018). This allows reducing the presence of systematic biases caused by spectral interferences and/or instrumental limitations. In particular, the use of one separate mean radiance spectrum per detector row minimizes the presence of so-called stripes in the product typical of imager-type instruments such as OMI or TROPOMI. Here we compute those mean radiance spectra on a daily basis by averaging for each row all spectra located within the equatorial Pacific Ocean (15°S-15°N; 120°W-180°W).



The selected settings for the DOAS fits rely on the aforementioned past studies and are summarized in Table 1. The latest available cross-sections for species absorbing in the selected fitting window are included in the fit, i.e. O<sub>3</sub>, NO<sub>2</sub>, O<sub>2</sub>-O<sub>2</sub>, water vapour and liquid water in addition to glyoxal. Note that the water vapour cross-section is based on HITRAN2012 database (Rothman et al., 2013) as we found that the latest HITRAN2016 version (Gordon et al., 2017) led to poorer fit quality. Sensitivity tests have shown that the retrieved glyoxal SCDs are significantly impacted by the choice of the H<sub>2</sub>O cross-section but also of its temperature. Effective water vapour temperatures (computed as the mean of temperature profiles weighted by typical H<sub>2</sub>O concentration profiles) are generally close to our selected value in regions with high water vapour content. This high sensitivity nevertheless points to the importance of having accurate water vapour cross-section, especially in regards of its possible influence on glyoxal fields over oceans (Chan Miller et al., 2014) (see section 4.2.3). The temperature dependence of the NO<sub>2</sub> absorption is taken into account by including a second cross-section, taken as the difference between NO<sub>2</sub> cross-sections reported at 2 temperatures (220 and 294K) as proposed by Alvarado et al. (2014) and Chan Miller et al. (2014) for their respective OMI glyoxal products. Consistently with Alvarado et al. (2014), we found that fitting the liquid water optical depth in the glyoxal fitting window performs as well as fixing it to a value previously determined in a larger spectral interval as proposed in the past (Lerot et al., 2010) with a limited presence of systematically negative glyoxal columns over remote oceans. Vibrational Raman scattering on remote ocean water also introduces some spectral structures caused by the filling-in of Fraunhofer lines. However, (Peters et al., 2014) have shown the simultaneous fit of the liquid water cross-section and of an intensity offset (see below) efficiently considers all remote ocean-related structures. A number of additional cross-sections are included in the fit to consider (1) Inelastic scattering (Ring effect) introduces high-frequency structures that are treated as a pseudo-absorber (Chance and Spurr, 1997); (2) Intensity offsets in the spectra, caused for example by residual straylight, are corrected for by fitting the inverse of the reference spectrum (Danckaert et al., 2017); (3) heterogeneity of the scene brightness may also introduce high frequency structures, which are considered with pseudo-cross-sections (more details hereafter). All those cross-sections are generated at the instrumental spectral resolution by using the key data Instrumental Spectral Response Functions provided for all individual detector rows. During the DOAS procedure, the earthshine radiance spectrum is further aligned with the reference, by allowing it to be shifted and stretched in wavelength. In addition, the DOAS fit procedure includes a spike removal scheme as described in Richter et al. (2011) enabling to filter out from the fit individual corrupted radiance measurements, and hence to reduce the noise in the product.

**Table 1 : Absorption cross-sections and settings used for the retrieval of glyoxal slant columns**

Fitting interval	435-460 nm
Absorption cross-sections	
Glyoxal	Volkamer et al. (2005)
Ozone	Serdyuchenko et al. (2014), 223K, <i>I<sub>0</sub> effect-corrected</i> (Aliwell et al., 2002)
NO <sub>2</sub>	Vandaele et al. (1998), 220K and 294K, <i>I<sub>0</sub> effect-corrected</i> (Aliwell et al., 2002)
O <sub>4</sub> (O <sub>2</sub> -O <sub>2</sub> )	Thalman and Volkamer (2013), 293K

H <sub>2</sub> O (vapour)	Rothman et al. (2013), 293K
H <sub>2</sub> O (liquid)	Mason et al. (2016)
Scene Heterogeneity	2 pseudo-absorbers (Richter, 2018) – Internally generated
Ring effect	Pseudo-absorber (Chance and Spurr, 1997; Wagner et al., 2009)
<b>Other parameters</b>	
Polynomial	3rd order
Intensity offset correction	1 <sup>st</sup> -order offset (additional cross-section taken as the inverse of the reference spectrum)
Earthshine wavelength shift	1 <sup>st</sup> -order shift
<b>Reference spectrum (<math>E_0</math>)</b>	Daily average of radiances, per detector row, selected in equatorial Pacific (Lat: [-15° 15°], Long: [180°-240°])

### 3.1.1. Scene heterogeneity

Any intensity variation within the probed scene taking place perpendicularly to the instrumental slit (i.e. along track) leads to perturbations of the instrumental spectral slit function (ISRF) (Noël et al., 2012; Voors et al., 2006). Richter et al. (2018) have shown that those perturbations lead to a degradation of the NO<sub>2</sub> DOAS spectral fit quality and to systematic biases on the retrieved slant columns. Such abrupt intensity changes occur for example along the coasts, mountains or cloud edges. Glyoxal retrievals are also affected by such scene heterogeneity as illustrated in Figure 2 over the Horn of Africa and Middle East. This figure shows in the panel (a) that the root mean square (RMS) of the DOAS fit residuals is systematically higher along the coasts but also over land where contamination by broken clouds or abrupt elevation changes cause discontinuities in brightness fields. The stripes visible in this figure are due to the smaller pixel size (and hence lower signal-to-noise ratio) on the edges of the across-track field of view. The panel (c) shows that there are some collocated artificial patterns (positive/negative biases) in the mean retrieved glyoxal slant column field. The latter result from spectral interferences with the signature introduced by the ISRF distortion. Richter et al. (2018) showed that those spectral interferences can be significantly reduced with additional cross-sections in the DOAS fit scaling the possible scene heterogeneity signature. Those cross-sections are generated with a statistical analysis of the fit residuals for many observations in a remote region of the Pacific Ocean as a function of the level of scene heterogeneity. The latter can be computed using radiance measurements at higher spatial resolution available in the TROPOMI level-1 data at a limited number of wavelengths. It ranges between -1 and +1 and is close to/deviates from 0 for homogenous/heterogeneous scenes, the sign indicating the part of the ground pixel that dominates the scene brightness. Following this approach, two additional cross-sections corresponding to the systematic residuals of scenes with an heterogeneity factor larger/smaller than +/- 0.08 have been added to the DOAS baseline and both the fit residuals and the identified glyoxal biases have been reduced as illustrated in the right panels (b) and (d) of Figure 2. This effect is particularly visible along coasts and mountains but also over lands where some pseudo-noise caused by persistent broken clouds is also largely reduced. Although significantly correlated, including the two heterogeneity cross-sections leads to a further improvement of the fit quality, likely due to a slit function perturbation that depends on the radiance distribution within the nominal ground pixel. Note that a third cross-

section derived from the mean residuals of homogeneous scenes is also added, which explains why the fit RMS are also reduced (but less drastically) in homogeneous scenes. This cross-section has no impact on the retrieved glyoxal SCDs and allowed mostly isolating systematic residuals due to scene heterogeneity only for the pseudo cross-sections creation.

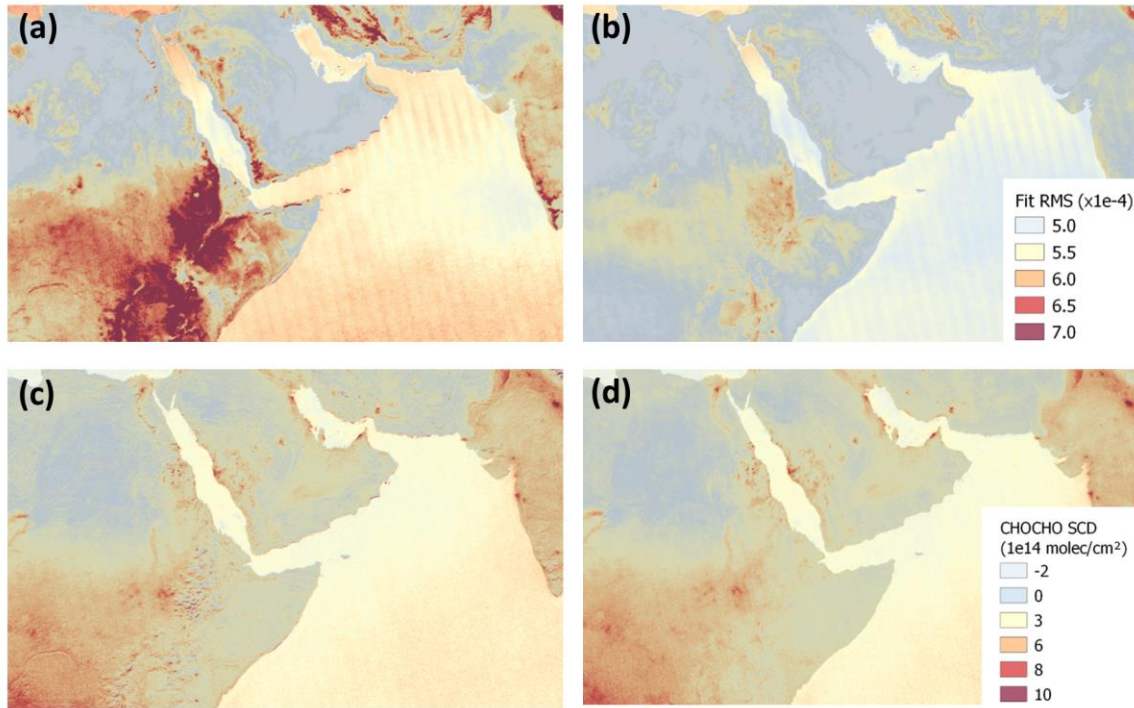


**Figure 2 : Impact of scene brightness heterogeneity on glyoxal retrievals in the fitting window 435-460 nm over the Horn of Africa and Middle-East. The panels (a) and (b) show mean fit residuals RMS for the year 2019 without and with (left and right) pseudo-cross sections to correct for spectral signatures introduced by scene heterogeneity. The panels (c) and (d) show the corresponding mean glyoxal slant column densities. Only observations with cloud fractions less than 20% are considered.**

### 3.1.2. Empirical correction for strong NO<sub>2</sub> absorption

The DOAS approach assumes that the wavelength dependence of the effective light path within the fit interval can be neglected. Although this assumption is generally reasonable, it may fail in case of strong absorption by one (or more) species, of which the slant column density becomes dependent on the wavelength (Pu $\acute{c}$ ite et al., 2010). In that case, fitting the optical depth of that species by a simple scaling of its cross-section is inaccurate and the fit quality is degraded. Pu $\acute{c}$ ite et al. (2010) have shown that fitting additional cross-sections resulting from a Taylor expansion of the wavelength-dependent slant column corrects for its variability within the fit window. As mentioned before, the high sensitivity of glyoxal retrievals to potential sources of misfit was a motivation to further investigate its sensitivity to extreme NO<sub>2</sub> concentration levels.

For this purpose, synthetic spectra were generated at a spectral resolution of 0.5 nm with the radiative transfer model SCIATRAN (Rozanov et al., 2005) for a satellite nadir-viewing geometry and two different solar zenith



angles. In those simulations, inelastic scattering was neglected and a large range of tropospheric NO<sub>2</sub> columns was covered by scaling the NO<sub>2</sub> a priori profile. The TROPOMI DOAS baseline described above was then applied to those simulated spectra in order to retrieve CHOCHO SCDs and evaluate the error as a function of the NO<sub>2</sub> SCD as illustrated in Figure 3. Results clearly point to a CHOCHO SCD error increasing with the NO<sub>2</sub> SCD. Note that the exact error magnitude may change slightly depending on the NO<sub>2</sub> vertical distribution and on the actual atmospheric content. On the other hand, adding ~~two~~ so-called Pukite cross-sections (Puķīte et al., 2010) ~~resulting from a first order expansion of the NO<sub>2</sub> slant column around the wavelength and the vertical optical depth to account for the wavelength dependence of the NO<sub>2</sub> SCD~~ significantly reduces the errors.

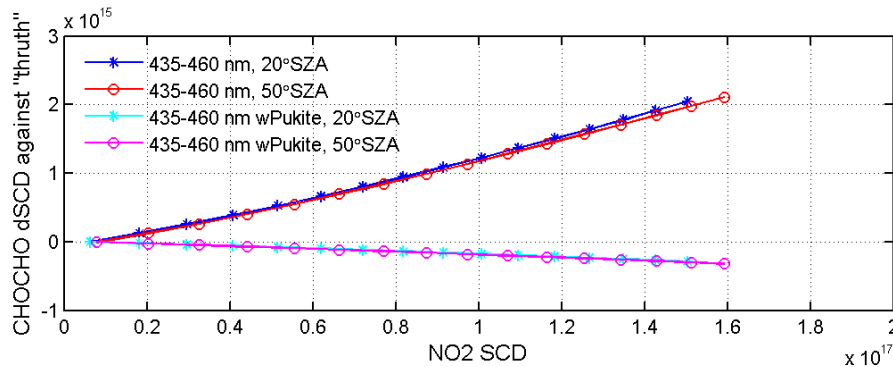


**Figure 3 : Absolute error (in molec/cm<sup>2</sup>) on the retrieved CHOCHO SCD as a function of the NO<sub>2</sub> SCD for simulated spectra in a nadir-viewing satellite geometry and for two solar zenith angles. The reference “true” CHOCHO SCD is taken as the value retrieved for the lowest NO<sub>2</sub> SCD scenario. The error increases with the NO<sub>2</sub> SCD when Pukite cross-sections are not included in the fit, but remains small otherwise.**

On this basis, the impact of adding the Pukite cross-sections to the DOAS baseline has been investigated using one month of TROPOMI data. A wintertime period was chosen (December 2019) to favour the number of observations with large NO<sub>2</sub> concentrations, in particular in China but also in other megacities in the Northern Hemisphere. Figure 4 (upper panel) displays the monthly mean NO<sub>2</sub> SCDs in December 2019, and (middle panel) the mean impact on the retrieved CHOCHO SCDs of introducing the Pukite terms in the DOAS spectral fit baseline. The CHOCHO SCD differences caused by the Pukite terms are also plotted as a function of the NO<sub>2</sub> SCDs to better visualize the correlation (lower panel). For regions with enhanced NO<sub>2</sub> concentrations (>2x10<sup>16</sup> molec/cm<sup>2</sup>) (e.g. China, India, Teheran), the Pukite cross-sections lead to a systematic reduction of the CHOCHO SCDs, consistent with the closed-loop tests described above. A small improvement of the fit quality is found (not shown). Unexpectedly, the impact of those additional cross-sections on the CHOCHO SCDs can also be non-negligible in regions with low NO<sub>2</sub> columns: positive differences are for example observed over equatorial oceans, but also over South America and Africa. The correlation plot of Figure 4 clearly shows these two regimes. While the impact of the Pukite cross-sections on the glyoxal retrievals is understood and reliable for large NO<sub>2</sub> SCDs, their influence at low NO<sub>2</sub> SCD is more questionable and likely results from spectral interferences occurring between the different fitted spectra (e.g. with the Ring signature), which introduces additional noise in the product.

To avoid this, rather than fitting additional cross-sections, we introduce an empirical correction applied to the glyoxal SCDs. This correction consists in subtracting from the glyoxal SCD a NO<sub>2</sub>-SCD dependent value, directly

prescribed from the linear regression fit through the sensitivity test results for all observations worldwide from December 2019, with NO<sub>2</sub> SCDs larger than  $2 \times 10^{16}$  molec/cm<sup>2</sup> as illustrated in Figure 4 (c). It is worth noting that the regression fit results agree well with the glyoxal SCD errors estimated from the simulations presented above (Figure 3). For extreme pollution conditions such as what can be found in China during Wintertime, this correction may lead to glyoxal column reduction up to 30%.

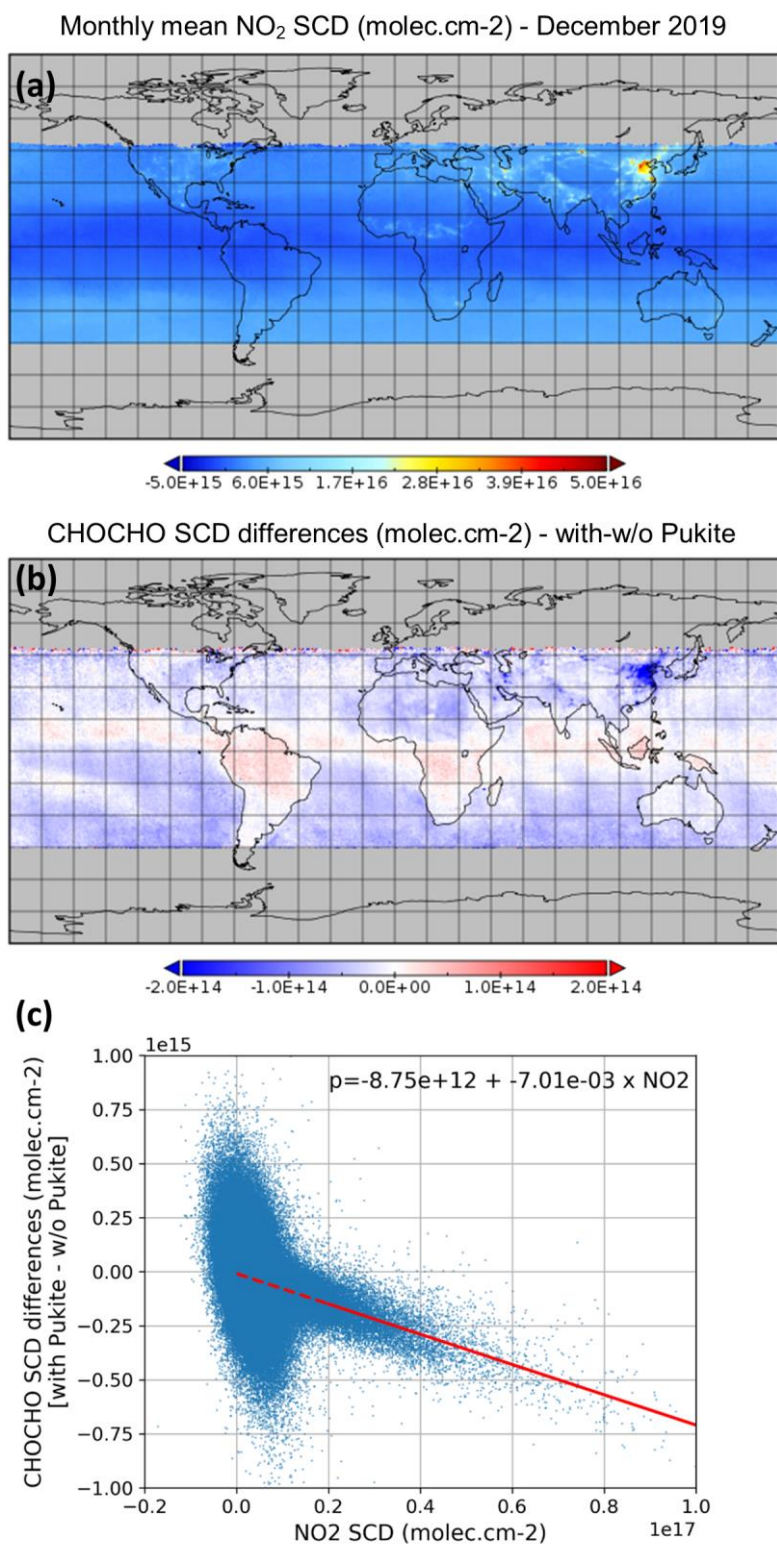


**Figure 4 : (a) Monthly mean NO<sub>2</sub> SCDs retrieved from TROPOMI data in December 2019. Panel (b) illustrates the CHOCHO SCD absolute differences (molec/cm<sup>2</sup>) due to the incorporation of the Pukite et al. (2010) cross-sections in the DOAS spectral fit and panel (c) shows the correlation between those differences and the NO<sub>2</sub> SCDs. The red line corresponds to a linear regression fit through all points with NO<sub>2</sub> SCD larger than  $2 \times 10^{16}$  molec/cm<sup>2</sup>.**

### 3.2. Air Mass Factor computation

The computation of the air mass factor (AMF) used to convert the retrieved glyoxal slant columns (SCD) to vertical columns (VCD) relies on the formulation of Palmer et al. (2001), which decouples the radiative transfer through the atmosphere from the vertical distribution of the gas of interest. Radiative transfer simulations are performed with the vector model VLIDORT at the middle of the fitting window (448 nm) to compute so-called altitude-dependent air mass factors or box-AMFs representing the sensitivity of the slant column to a small concentration change at any altitude. The AMF is obtained as the weighted mean of those box-AMFs using as weights the vertical distribution of the glyoxal concentration.

Typically, the sensitivity of nadir-viewing UV-Visible instruments is reduced in the lowermost atmospheric layers because of Rayleigh scattering. However, this sensitivity depends strongly on the observation geometry, on the surface reflectivity and altitude and on the presence of clouds. For example, the sensitivity is generally further reduced for low sun elevation. For this reason, retrievals with solar zenith angles larger than 70° are filtered out. We use a pre-computed five-dimensional look-up table of Box-AMFs spanning all observation conditions (see Table 2) and from which appropriate values are linearly interpolated for every TROPOMI observation. This interpolation uses as input the observation angles provided in the level-1 data, surface elevation taken from the GMTED2010 topography (Danielson and Gesch, 2011) and surface albedo extracted from the OMI minimum Lambertian Equivalent Reflectivity climatology (Kleipool et al., 2008). The spatial resolution of the latter database (0.5°x0.5°) is coarse compared to the TROPOMI footprint and neglects anisotropy, which may introduce significant errors (Lorente et al., 2018). However, at the time of writing, it is the only database available at the S5p overpass time although new Lambertian Equivalent Reflectivity climatologies relying on past works (e.g. Loyola et al., 2020; Tilstra et al., 2021, 2017) are currently being prepared. On the other hand, the level of noise in glyoxal retrievals generally requires averaging in space and/or time which in turn will reduce part of those error sources. We also neglect the impact of clouds and aerosols on the radiative transfer. Instead we apply a stringent cloud filtering approach: only observations with an effective cloud fraction (as retrieved in the same spectral range and provided in the TROPOMI operational NO<sub>2</sub> product (van Geffen et al., 2019) lower than 20% are conserved. This approach is motivated by the fact that glyoxal slant columns tend to be biased high over bright scenes because of poorly understood residual spectral interferences (e.g. with the Ring signature). Similarly, scenes covered by snow and ice are also discarded.

Table 2 : Granularity of the Box-AMF look-up table

Parameter name	Grid of values
Solar zenith angle [deg]	0, 10, 20, 30, 40, 45, 50, 55, 60, 65, 70, 72, 74, 76, 78, 80, 85
Line of sight zenith angle [deg]	0, 10, 20, 30, 40, 50, 60, 65, 70, 75
Relative azimuth angle [deg]	0, 45, 90, 135, 180
Surface albedo	0, 0.01, 0.025, 0.05, 0.075, 0.1, 0.15, 0.2, 0.25, 0.3 0.4, 0.6, 0.8, 1.0
Surface pressure [hPa]	1063.10, 1037.90, 1013.30, 989.28, 965.83, 920.58, 876.98, 834.99, 795.01, 701.21, 616.60, 540.48, 411.05, 308.00, 226.99, 165.79, 121.11

332

333 The Typical monthly-dependent a priori glyoxal vertical profile shapes necessary to perform the AMF  
334 computations are have been calculated provided at the different satellite overpass times by with the global  
335 Chemistry Transport Model MAGRITTE developed at BIRA-IASB, which inherits from the IMAGES model  
336 (Bauwens et al., 2016; Müller and Brasseur, 1995; Stavrakou et al., 2009b, 2013). This model runs at  $1^\circ \times 1^\circ$   
337 resolution and calculates the distribution of 182 chemical compounds, of which 141 species undergo transport.  
338 The modelled troposphere is vertically divided in 40 levels between the surface and the lower stratosphere and  
339 meteorological fields are provided by the ECMWF ERA-5 analyses. The chemical mechanism and deposition  
340 scheme have been recently updated (Müller et al., 2018, 2019). Anthropogenic NMVOC emissions of are  
341 provided by the EDGAR 4.3.2 inventory (Huang et al., 2017) for the year 2012. Biomass burning emissions are  
342 obtained from the Global Fire Emission Database version 4 (GFED4s) (Van Der Werf et al., 2017). The emissions  
343 of isoprene and monoterpenes are calculated using the MEGAN-MOHYCAN model (Guenther et al., 2012;  
344 Müller et al., 2008). The model also incorporates biogenic emissions of methanol, methyl-butenol, ethylene,  
345 ethanol, acetaldehyde, formaldehyde and acetone, as well as oceanic emissions of methanol, acetone, acetaldehyde  
346 and alkyl nitrates (Müller et al., 2019). The global source of glyoxal in the model amounts to 47 Tg/yr (in 2013),  
347 of which about 4 Tg/yr are due to direct biomass burning emissions, and 18, 6, 9 and 9 Tg/yr are due to the  
348 atmospheric degradation of isoprene, acetylene, aromatics and monoterpenes, respectively (Müller et al., 2019).

349 To account for the difference in spatial resolution between the model and the observations, a priori profiles are  
350 rescaled to the effective satellite pixel surface elevation using the formulation proposed by Zhou et al. (2009).  
351 Enhanced glyoxal concentrations have been detected over oceans in several studies (Coburn et al., 2014; Lerot et  
352 al., 2010; Sinreich et al., 2010), but current models cannot reproduce this. For this reason, over oceans, we use an  
353 a priori glyoxal concentration profile measured with an air-borne MAX-DOAS instrument over the Pacific Ocean  
354 during the TORERO campaign (Volkamer et al., 2015).

### 3.3. Background correction

As already mentioned, systematic (row-dependent) biases in the retrieved SCDs often remain due to small residual interferences with spectral signatures from other absorbers or due to instrumental effects. In the particular case of pushbroom imaging instruments such as OMI/TROPOMI, across-track row-dependent biases (so-called stripes) often occur due to the imperfect calibration of the different CCD detector rows. To reduce those biases, a background correction using observations in a remote reference sector is generally applied as part of the retrieval algorithm (e.g. Alvarado et al., 2014; Chan Miller et al., 2014; Lerot et al., 2010; Richter and Burrows, 2002; De Smedt et al., 2018). The principle of this background correction is to add offset values to the retrieved SCDs to ensure that the resulting mean VCD in a clean remote region match an a priori known tropospheric glyoxal column. Here we use the Pacific Ocean as reference sector with a constant reference VCD of  $1 \times 10^{14}$  molec/cm<sup>2</sup>. This value was chosen according to independent measurements performed in this region (Sinreich et al., 2010) since current global models fail to reproduce remote sensing glyoxal levels observed over oceans (Fu et al., 2008; Myriokefalitakis et al., 2008; Stavrou et al., 2009b). There is nevertheless an uncertainty related to this reference value, which impacts the overall level of the product. This error component is further discussed in section 3.4.3 and is taken into account to estimate the total glyoxal VCD error. As all intermediate variables (SCD, corrected-SCD, AMF) are provided in the product, a user could recompute glyoxal VCDs using a different reference Pacific value.

The background correction is applied on a daily basis in different steps:

1. First, a destriping procedure such as proposed in Boersma et al. (2007) is applied consisting in an offset correction determined separately for each instrumental row, and relying on clear sky observations from the Equatorial Pacific Ocean (15°S-15°N, 165°E-220°E). The offset corrections are added to all glyoxal SCDs worldwide, considering their respective row.
2. Additionally to the high frequency stripes, a broadband row-dependent structure, of which the shape also depends on the latitude, was identified as illustrated in Figure 5, panel (a). This figure compares the row-dependence of mean uncorrected VCDs in the Pacific Ocean at Equatorial and Northern mid-latitudes. The two curves are somehow anti-correlated, meaning that the destriping correction based on equatorial latitudes only as applied in step 1 is not sufficient and even reinforces the mid-latitude structure. The second step of the background correction aims thus at reducing this broadband row-dependent structure at all latitudes while maintaining the mean latitudinal distribution of the measured background glyoxal columns. For this, Pacific Ocean measurements (40°S-40°N, 165°E-220°E) are binned per 20° in latitude and in groups of 15 rows in a 2-dimensional matrix. For this step, we use reference VCDs depending on the latitude and resulting from the averaging of the binned VCDs along the row dimension. A corresponding 2-dimensional matrix of SCD offset corrections is then computed in order, once applied to the binned VCDs, the corrected values match the reference VCDs. Interpolation through this correction matrix provides offsets to be applied to all SCDs retrieved worldwide. For satellite pixels out of the latitude range, no extrapolation is performed but instead, the nearest neighbour correction values are taken.
3. Finally, the overall level of the product is adjusted with a single offset correction to ensure that the mean of all clear-sky VCDs within the full reference sector (40°S-40°N, 165°E-220°E) is equal to  $1 \times 10^{14}$



molec/cm<sup>2</sup>. Panel (b) of Figure 5 shows how the identified row dependence in the VCDs at different latitudes has been reduced. The general level of the columns has also been adjusted.

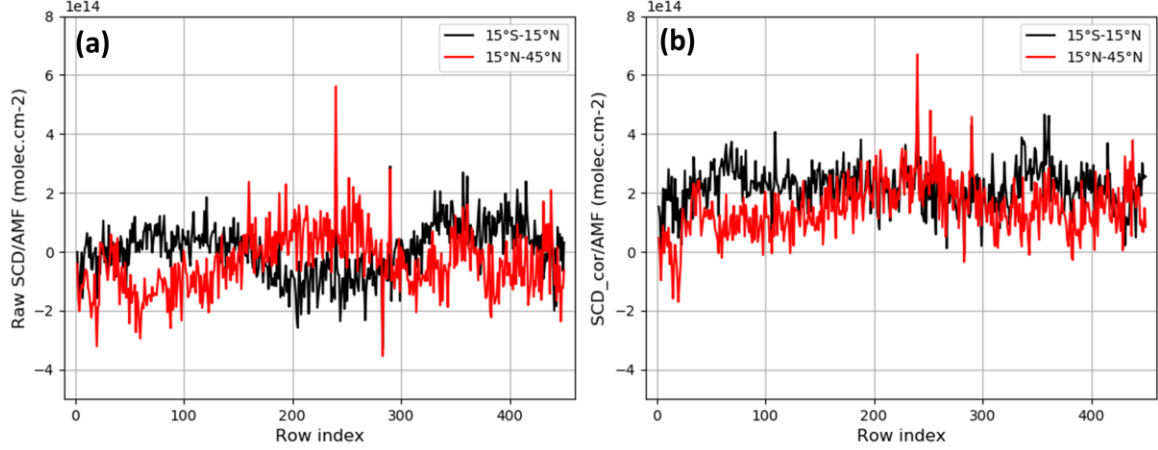


**Figure 5 : Row-dependence of the glyoxal vertical columns of S5p orbit #5877 (December, 1st 2018) averaged in an equatorial latitude band and in a Northern mid-latitude band. (a) No background correction is applied; (b) a latitude-dependent background correction is applied.**

### 3.4. Uncertainty estimates

Glyoxal tropospheric column retrievals are affected by many sources of uncertainties in the different components of the algorithm. The low glyoxal optical depth makes its retrieval highly sensitive to measurement noise and to spectral interferences with strong absorption signatures of other species or with instrumental features. Although the measurement noise can be reduced by averaging column retrievals from individual observations, spectral interferences generally lead to residual systematic errors (biases), which cannot be easily eliminated. The background correction described above aims at reducing those biases, but it has its own limitations. For example, the reference glyoxal tropospheric column within the reference sector is poorly known. In addition to spectral fit errors, there are also significant errors associated to the air mass factor calculations, mostly originating from input parameters uncertainties. For estimating the total glyoxal column error, we assume that the different error components are uncorrelated and can be summed quadratically as in (Boersma et al., 2011; Lerot et al., 2010; De Smedt et al., 2008, 2018). If the glyoxal vertical column  $N_v$  is expressed as

$$N_v = \frac{N_s - \overline{(N_{s,0} - N_{v,0,ref} \times M_0)}}{M} \quad (1)$$

with  $N_s$  the retrieved slant column,  $M$  the AMF,  $\overline{(N_{s,0} - N_{v,0,ref} \times M_0)}$  the background correction term where  $N_{s,0}$ ,  $M_0$ ,  $N_{v,0,ref}$  are the slant columns, AMF, and the reference vertical column within the reference sector, the total glyoxal vertical column error can be written as

$$\sigma_{N_v}^2 = \frac{1}{M^2} \left( \sigma_{N_s}^2 + N_v^2 \sigma_M^2 + \sigma_{N_{s,0}}^2 + N_{v,0,ref}^2 \sigma_{M,0}^2 + M_0^2 \sigma_{N_{v,0,ref}}^2 \right) \quad (2)$$

where  $\sigma_{N_s}$ ,  $\sigma_M$  and  $\sigma_{N_{v,0,ref}}$  are the errors on the slant column, the air mass factor and the reference value used in the background correction, respectively. In the following subsections, we discuss the different contributions to each of those terms. Errors can affect the retrievals randomly or systematically (biases). While the main random error is caused by the propagation of the instrumental photon detector shot noise on the measured radiances, the other error components are considered as being systematic. It has however to be noted that the latter assumption may lead to conservative systematic error estimates and to an underestimation of the product scatter, depending on the time and spatial resolution of interest. In particular, uncertainties associated to the input parameters needed for the AMF calculation are directly related to the resolution of the used databases and may appear as random at coarser resolution. This has been discussed by (Vigouroux et al., 2020) who attributed part of the scatter in formaldehyde vertical column TROPOMI/MAX-DOAS differences to a random component of the AMF errors.

### 3.4.1. Slant column uncertainties

As mentioned above, the radiance measurement noise directly propagates into the glyoxal slant column retrieval and leads to large random errors  $\sigma_{N_{s,rand}}$  (or precision) due to the low glyoxal optical depth. Those are easily estimated using the fit residuals RMS and the covariance matrix of the cross-sections included in the fit (Danckaert et al., 2017). In the visible spectral range, the TROPOMI signal-to-noise ratio is about 1600 over dark scenes. This leads to a glyoxal VCD precision (i.e.  $\sigma_{N_{s,rand}}/\text{AMF}$ ) in the range of 6-10x10<sup>14</sup> molec/cm<sup>2</sup> as illustrated in Figure 6, panel (d). This range of values is consistent with the scatter observed in the retrieved glyoxal SCDs in regions without any significant glyoxal source. Over bright scenes, for example covered by clouds or snow, those errors significantly drop because of the increased signal-to-noise ratio. For individual observations, random errors dominate and averaging is needed to extract meaningful glyoxal signals.

There are also systematic errors associated to the DOAS spectral fit that are mainly dominated by absorption cross-section uncertainties, by interferences with other species (O<sub>4</sub>, liquid water, Ring ...), or by other effects such as residual stray light. Those contributions are difficult to assess and can only be estimated from sensitivity tests (Lerot et al., 2010). In general, this error term can be as high as 2-3x10<sup>14</sup> molec/cm<sup>2</sup>. However, the use of a radiance as reference in the DOAS fit and the application of a background correction removes a large part of the systematic error in the slant column fit (see section 3). As those corrections are not always sufficient to eliminate completely the SCD systematic errors due to local conditions (local pollution, residual clouds,...), we set  $\sigma_{N_{s,syst}}$  to 1x10<sup>14</sup> molec/cm<sup>2</sup>.

### 3.4.2. AMF uncertainties

The errors on the air mass factor depend on the input parameter uncertainties and on the sensitivity of the air mass factor to each of them. This contribution can be broken down into the squared sum (Boersma et al., 2011; Lerot et al., 2010; De Smedt et al., 2018) as

$$\sigma_{M,syst}^2 = \left( \frac{\partial M}{\partial A_s} \cdot \sigma_{A_s} \right)^2 + \left( \frac{\partial M}{\partial S} \cdot \sigma_S \right)^2 + (0.15M)^2 \quad (3)$$

where  $\sigma_{A_s}$  and  $\sigma_S$  are typical uncertainties on the surface albedo and profile shape, respectively.

The contribution of each parameter to the total air mass factor error depends on the observation conditions. Therefore, a small table of air mass factor derivatives spanning all observation conditions was computed using VLIDORT, considering glyoxal box profile shapes with different effective heights.

The AMF error component related to the surface reflectivity (1<sup>st</sup> term of Eq. (3)) is calculated using an estimated uncertainty on the albedo  $\sigma_{A_s}$  of 0.02 (Kleipool et al., 2008). Note that this uncertainty can be occasionally larger, in particular at high latitudes where snow falls may cause abrupt changes in scene albedo. The uncertainty associated to the a priori profile shapes (the smoothing error) used in the retrieval is more difficult to assess, especially due to the scarcity of independent glyoxal profile measurements. For every observation, an effective height corresponding to the a priori glyoxal profile used in the AMF calculation is derived and used to extract the appropriate AMF derivative and  $\sigma_s$  is taken equal to 50hPa. The latter value corresponds to the typical standard deviation of the model profile shape effective heights over polluted regions.

Formulation (3) is valid for clear sky pixels and the stringent cloud filtering we use. However, residual clouds undoubtedly impact the radiative transfer and generally shield the lowermost atmospheric layers. Therefore, we anticipate that the clear sky assumption generally leads to a low bias on the retrieved glyoxal columns in case of residual clouds. On the other hand, the spectral interferences over bright (cloudy) scenes as discussed in section 3.2 impact the retrievals the other way round. The third term in equation (3) accounts for possible errors in the AMF model itself, including the neglect of aerosols and clouds, wavelength dependence,..., and is estimated to be 15% of the air mass factor (Lorente et al., 2017).

### 3.4.3. Background correction uncertainties

Although the background correction is designed to overcome systematic features/deficiencies of the slant column fitting, some errors are also associated to this procedure. In particular, systematic errors on the reference slant columns and their air mass factors are propagated into the computed correction values. Also, there is an uncertainty related to the reference glyoxal vertical column value in the reference sector as mentioned in section 3.3. The three last terms of Eq. (2) represent the total background correction uncertainty in which  $\sigma_{N_{s,0}}$  is the systematic slant column error fixed to  $1 \times 10^{14}$  molec/cm<sup>2</sup> (see above section 3.4.1 (6.5.1)), and  $M_0$  and  $\sigma_{M_0}$  are the air mass factors and their associated errors within the reference sector. In practice, those quantities are treated similarly as the reference slant columns (i.e. binned in latitude and row bins – see section 3.3).  $\sigma_{N_{v,0,ref}}$  represents the error associated to the reference value  $N_{v,0,ref}$  and is fixed to  $5 \times 10^{13}$  molec/cm<sup>2</sup>. Using a different reference value would directly impact the overall level of glyoxal VCDs worldwide, with some small modulations related to the ratio of the AMFs over Pacific and in other regions following Eq. (1).

### 3.4.4. Total systematic uncertainties

Figure 6, panel (c) shows the estimated mean VCD systematic errors for the month of June 2018 when all systematic error sources are combined together using Eq. (2). Note that the conversion of the AMF error into an absolute vertical column error (2<sup>nd</sup> term of the equation) requires this error to be multiplied by the corresponding vertical column. Because of the high level of noise in the product, using the retrieved column for this would lead

to a strong overestimation of the systematic error. To circumvent this, we use instead pre-computed climatological glyoxal noise-free VCDs.

Total glyoxal VCD systematic errors are generally in the range  $1\text{--}3 \times 10^{14}$  molec/cm<sup>2</sup>, corresponding to about 30–70% for emission regimes (columns larger than  $2 \times 10^{14}$  molec/cm<sup>2</sup>). Figure 7 shows the zonally averaged total systematic error along with its different components for one S5p orbit passing over Africa. In general, the three components contribute similarly to the total error for emission conditions. On contrary, the AMF error becomes smaller in background conditions while the two other terms dominate. Note that pixels strongly contaminated by clouds (cloud fraction > 20%) or covered by snow/ice are discarded. Systematic errors are expected to be large for those pixels mainly due to spectral interference effects (see section 3.2) and also because the information content on glyoxal is reduced in case of cloud shielding. Figure 6, panel (b) shows monthly mean AMFs for the same month. Small AMFs are generally caused by a priori profiles peaking near the surface, which makes the retrieval more sensitive to albedo uncertainties and to a lesser extent to the a priori profile shape uncertainties. This explains the anti-correlation between the AMFs and the systematic errors. In contrast, large AMFs are caused either by bright surface or by background a priori profiles. For such cases, systematic errors are smaller. Note that satellite column averaging kernels, defined as the Box-AMF divided by the total AMF (Eskes and Boersma, 2003), are provided for every observation. They can be used to remove the smoothing error component when comparing the satellite data to any other external data.

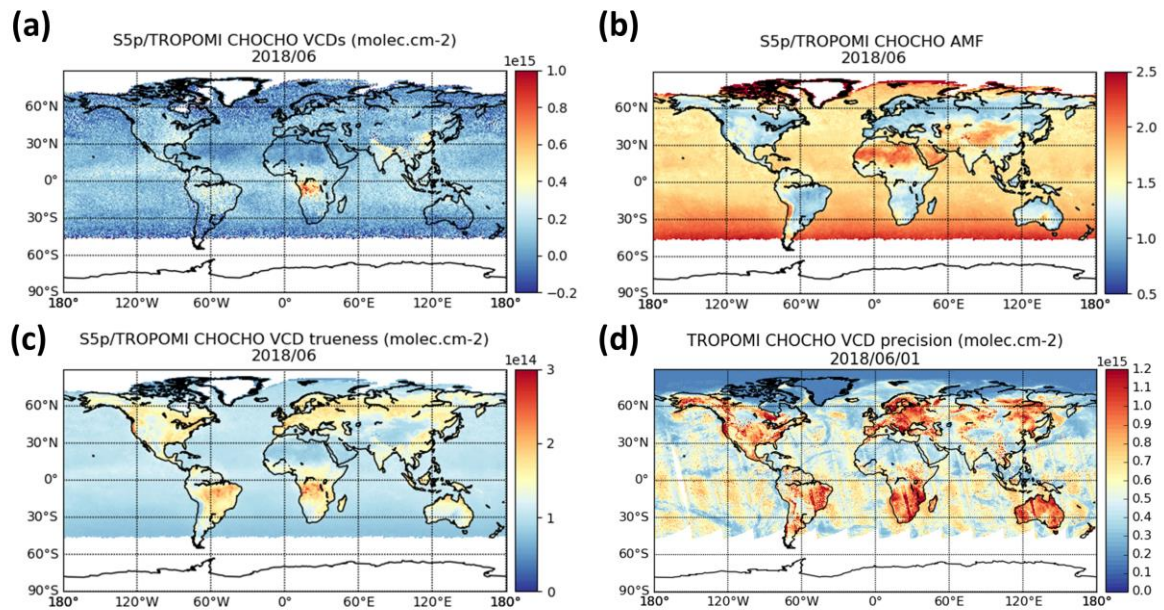


**Figure 6:** (a) TROPOMI June 2018 monthly means of glyoxal tropospheric columns, glyoxal air mass factors (panel (b)) and glyoxal tropospheric column systematic errors (panel (c)). Scenes contaminated by clouds or Ice/snow have been filtered out. Panel (d) shows glyoxal tropospheric column random errors for one single day, in which all observations have been kept to illustrate the impact of the scene brightness.

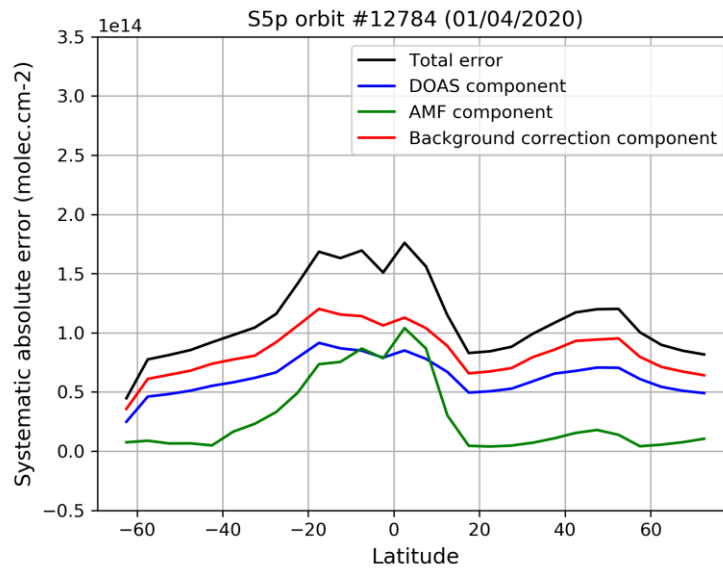


**Figure 7 : Zonal mean of the total glyoxal VCD systematic error along with its different components for one single S5p orbit passing over Africa on April, 1st 2020.**

#### 4. Comparison with other satellite instruments

##### 4.1. Algorithmic differences for GOME-2A/B and OMI glyoxal retrievals

Glyoxal tropospheric columns have also been retrieved from other satellite instruments, namely GOME-2 on board the platforms Metop-A and -B and OMI on board AURA. Retrieval settings very similar to those described in the previous section were applied. For GOME-2A and B, we use data records recently produced within the operational environment of the EUMETSAT AC SAF (Valks et al., 2020). We list here the remaining differences with respect to the TROPOMI algorithmic baseline and the specificities for each instrument.

All data sets essentially share the same DOAS fit settings (reference cross-sections, fit window, polynomial degree...). The heterogeneity cross-sections are omitted for the GOME-2 and OMI retrievals. While the instrumental design of GOME-2 makes it weakly sensitive to scene heterogeneity, it would be beneficial for OMI to include similar cross-sections but that would imply a reprocessing of the complete slant column data set data with limited added-value for the large-scale comparison with TROPOMI that we present in the next subsection. For the GOME-2 instruments, we also fit two additional cross-sections representative of the instrumental sensitivity to light polarization as provided from the level-1 key data (EUMETSAT, 2011) as well as one pseudo cross-section to account for an along-track spectral resolution change occurring due to instrumental temperature change (Azam and Richter, 2015). Note that for GOME-2 the cross-sections are convolved with an instrumental slit function optimized as part of the wavelength calibration for every measured irradiance (De Smedt et al., 2015), which allows accounting for the known long-term drift of the GOME-2 instrument spectral response function.

Differences in air mass factor calculations consist only in using, over land, a priori profiles provided by IMAGESv2, the chemical transport model predecessor of MAGRITTE, at the coarser resolution of  $2.0^\circ \times 2.5^\circ$ . For the GOME-2 instruments, we use the directionally dependent Lambertian-equivalent reflectivity database produced by Tilstra et al. (2021) instead of the OMI database.



A background correction procedure is applied consistently with the one used for TROPOMI. The GOME-2 instruments being whiskbroom scanners, there is no destriping procedure as such but instead a viewing zenith angle-dependent correction is applied, also relying on the slant columns retrieved in the Equatorial Pacific sector. This correction may account for example for remaining biases related to the instrumental polarization sensitivity. For both OMI and GOME-2, the row/VZA dependence does not show any obvious change along the orbit and the corresponding correction thus relies only on the low latitude measurements.

Note that the OMI and GOME-2 glyoxal products are filtered for cloudy scenes using cloud fraction lower than 20% as taken from the O<sub>2</sub>-O<sub>2</sub> (Veefkind et al., 2016) and OCRA (Lutz et al., 2016) cloud products, respectively. The empirical correction for strong NO<sub>2</sub> absorption signature described in section 3.1 has been applied to those instruments as well. In the following section, we compare the TROPOMI glyoxal retrievals with the OMI and GOME-2A/B data sets. The OMI record covers the period 2005-2018, while GOME-2A/B span the periods 2007-2017 and 2013-2020, respectively. OMI and GOME-2A records were interrupted when their respective quality was degraded too severely and other instruments were available to continue the morning and afternoon time series.

## **4.2. Glyoxal satellite inter-comparison**

### **4.2.1. Comparison of the noise level**

As mentioned before, the level of noise in the satellite glyoxal tropospheric column products is large compared to the real signal. This is illustrated in the upper panel of Figure 8 which shows all individual clear-sky TROPOMI glyoxal columns retrieved in the Pacific Ocean on June, 1<sup>st</sup> 2018 and plotted as a function of their latitude. The scatter is significant ( $\sigma \approx 5\text{-}7 \times 10^{14}$  molec/cm<sup>2</sup>) with respect to the small glyoxal VCDs averaged in 5°-latitude bins in this sector. The lower panel compares the standard deviation of the retrievals from TROPOMI, OMI, GOME-2A and B in the same remote sector for the 1<sup>st</sup> of June of their respective first year of operation. The scatter in the retrievals is directly linked to the instrumental signal-to-noise ratio, which is documented to be around 500 for OMI (Schenkeveld et al., 2017), 1000 for GOME-2 (Zara et al., 2018) and 1500 for TROPOMI (Kleipool et al., 2018). In practice, we see that the CHOCHO observation noise is indeed slightly larger for OMI, that GOME-2B retrievals are noisier than those from GOME-2A, which have a level of noise similar to TROPOMI. Considering the very small footprint size of TROPOMI (3x7.5 km<sup>2</sup> and 3x5.5 km<sup>2</sup> after August 2019) compared to the other instruments (GOME-2: 80x40 km<sup>2</sup>; OMI: 13x24 km<sup>2</sup> at nadir), the TROPOMI observation noise is remarkably low. More importantly, the much larger amount of TROPOMI data compared to OMI (~15x) and GOME-2 (~100x) allows maintaining a better time or spatial resolution for a given target noise level. For example, the random error associated to the daily glyoxal column averaged in an area defined by a circle with a radius of 50 km will be less than  $0.5 \times 10^{14}$  molec.cm<sup>-2</sup> for TROPOMI, while it will remain larger than  $2.5 \times 10^{14}$  molec/cm<sup>2</sup> and  $4.0 \times 10^{14}$  molec/cm<sup>2</sup> for OMI and GOME-2, respectively.

This is illustrated in Figure 9, which compares January monthly mean glyoxal VCD fields over Asia at the resolution of 0.05° for TROPOMI and OMI (upper panels) and 0.25° for GOME-2A and OMI (lower panels) after one year of their respective operation. At the resolution of 0.05°, the level of noise in the TROPOMI glyoxal map is very low and many details can be distinguished in the glyoxal spatial distribution. In particular, hot spots of glyoxal over many megacities are clearly identified (e.g. over Bangkok, New Delhi, Ho Chi Minh City,

Shenzhen...) but also over Cambodia where large fires occur every year from January to March. At this resolution of  $0.05^\circ$ , the level of noise in the OMI map remains high and prevents distinguishing such details. At the coarser spatial resolution of  $0.25^\circ$ , the reduction of the noise in the OMI and GOME-2 monthly glyoxal fields appears to be sufficient to better distinguish the glyoxal spatial distribution but at the cost of a significant smoothing. In the next section, we will intercompare the four satellite products at low temporal and spatial resolution in order to minimize the impact of the noise and to identify possible systematic discrepancies.

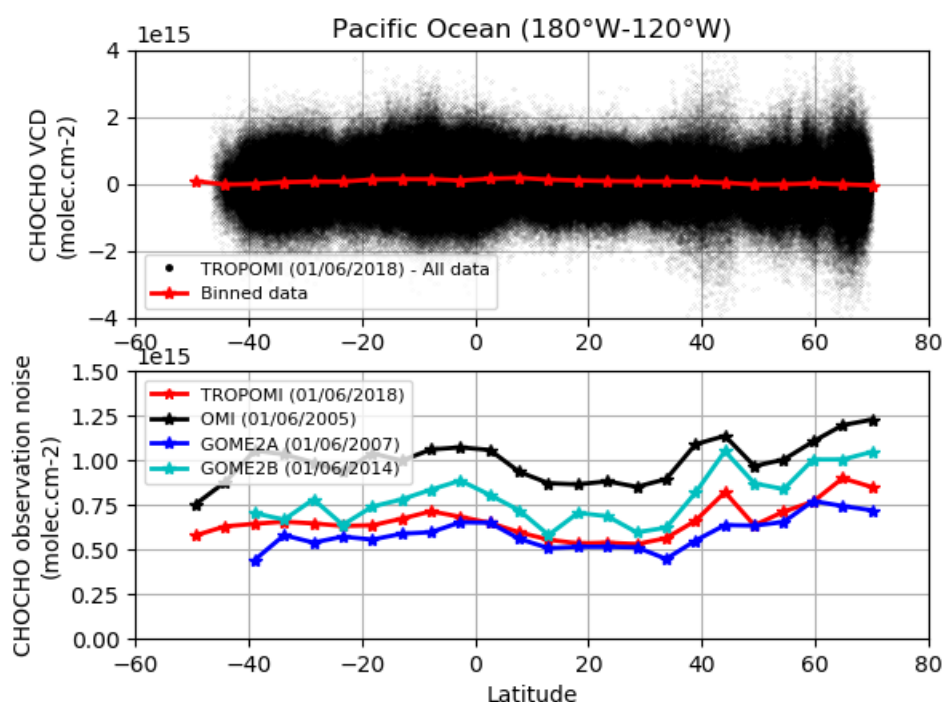


**Figure 8 : Illustration of the level of noise in satellite CHOCHO VCD retrievals. The upper panel shows all clear sky individual glyoxal VCDs retrieved in the Pacific Ocean from TROPOMI observations on June, 1st 2018. The scatter is very large compared to the low real signal as illustrated by the data binned in  $5^\circ$  latitude bands. The lower panel compares the standard deviation of the retrievals in the same sector from TROPOMI, OMI, and GOME2A/B on the 1st of June of their respective first year of operation.**

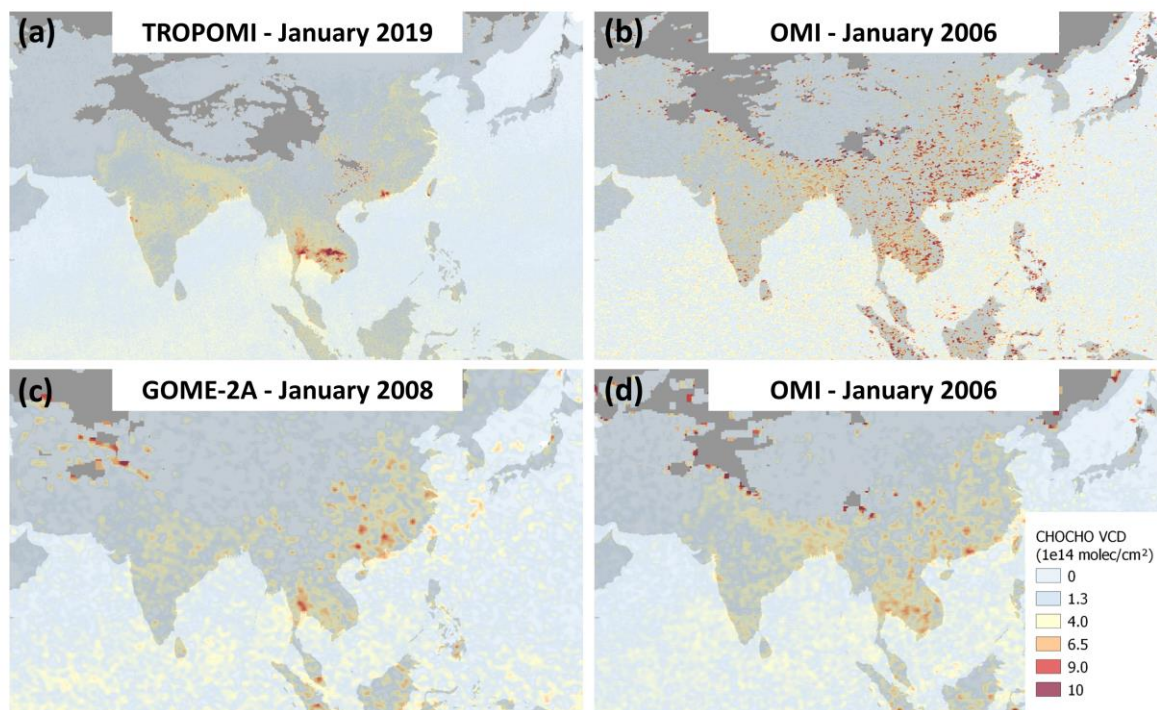


**Figure 9: Illustration of the impact of the instrumental signal-to-noise and available amount of data on monthly mean glyoxal VCD fields retrieved from different satellite instruments. The (a) TROPOMI data for January 2019 gridded at a resolution of  $0.05^\circ$ , (b) OMI data for January 2006 gridded at a resolution of  $0.05^\circ$ , (c) GOME-2A data for January 2008 gridded at a resolution of  $0.25^\circ$ , and (d) OMI data for January 2006 gridded at a resolution of  $0.25^\circ$ . Cloudy scenes have been filtered out and a smoothing filter has been applied on the four presented fields based on a spatial mean with the nearest neighbouring grid cells.**

#### 4.2.2. Comparison of mean glyoxal fields

First, Figure 10 and Figure 11 compare seasonal maps of glyoxal VCDs generated from TROPOMI, OMI and GOME-2A/B data products. In order to reduce the data scatter for each instrument, those maps are based on long time series as indicated in the figures. Therefore, a one-to-one match is not expected. As can be seen, the consistency between the four instruments is excellent. Glyoxal patterns are captured similarly for all seasons in terms of both spatial distribution and VCD values. The largest glyoxal columns are observed in tropical regions, where biogenic emissions are important, and in regions with important fire events (e.g. Amazonia and Northern Africa in SON, Thailand/Indochina in MAM, Western US in August,...). At mid-latitudes, the glyoxal columns follow the seasonal cycle of biogenic activity with maximum values during summertime. Localized hot spots of glyoxal are visible over megacities corresponding to strong anthropogenic emissions (e.g. Northern China Plain, Bangkok, Teheran, New Delhi, Sao Paulo...).

~~Also a persistent oceanic glyoxal signal is seen consistently by the four sensors. Note that a similar signal has been detected from ship and airborne MAX DOAS in the equatorial Pacific and Atlantic Oceans (Behrens et al., 2019a; Sinreich et al., 2010; Volkamer et al., 2015).~~ In contrast to TROPOMI and OMI, the level of noise in the GOME-2 data sets significantly increases over the South Atlantic Anomaly despite the application of a spike-removal procedure (section 3.1). Overall the GOME-2B maps are noisier than those from other sensors due to the

lower signal-to-noise ratio of the spectra and a shorter time series. Compared to the UV, the sensitivity to the surface is larger in the visible, which may introduce interferences with the spectral signature of specific ground surfaces, and thus may potentially lead to a bias on the retrieved columns. A striking example is over the Karabogaz-Gol near the Caspian sea, which is one of the saltiest lakes in the world and contains large concentrations of sediments (Kosarev et al., 2009). The glyoxal signal detected over that lagoon is unlikely to be physical and likely originates from interferences with the ground reflectance spectral signature.

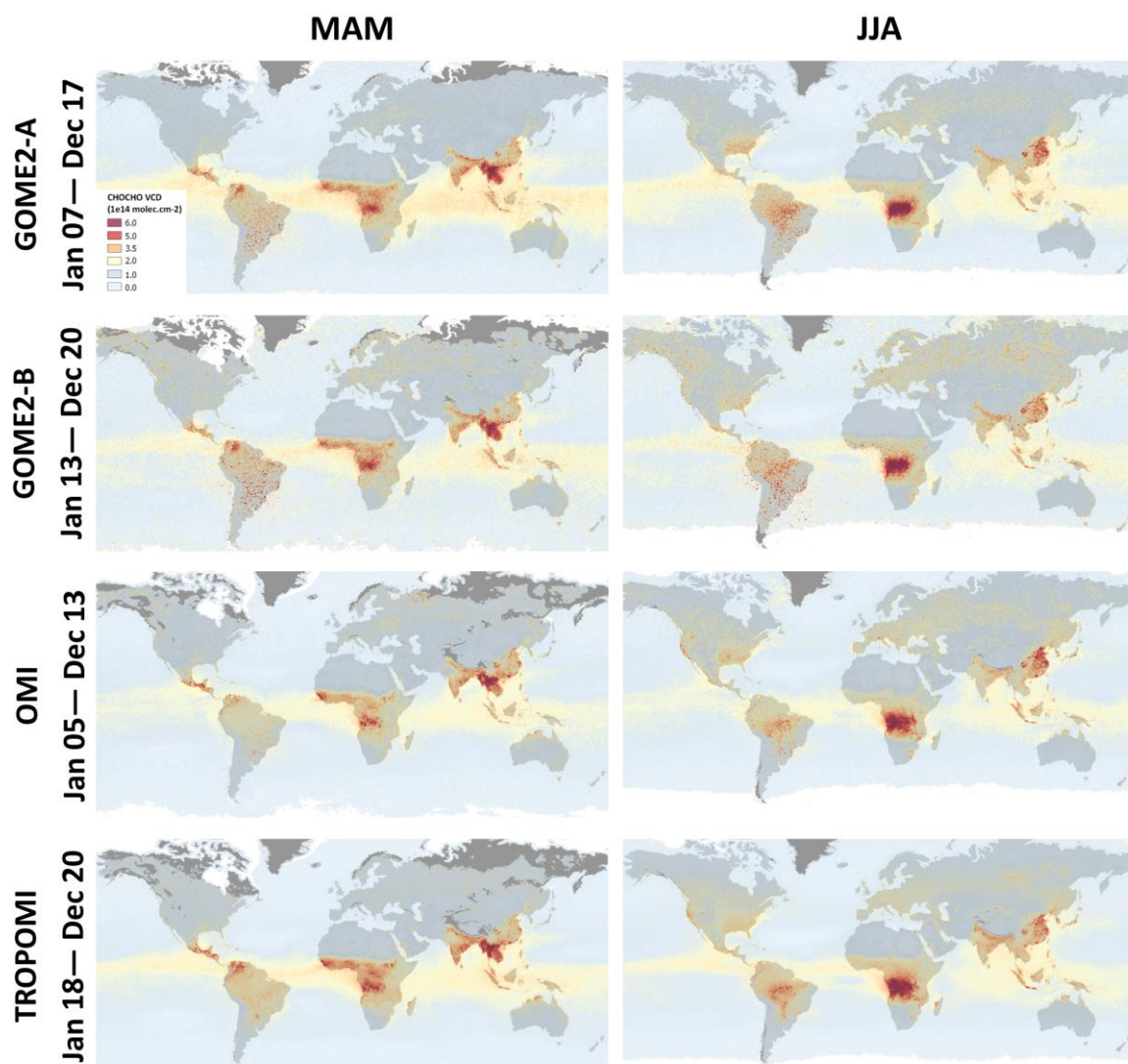
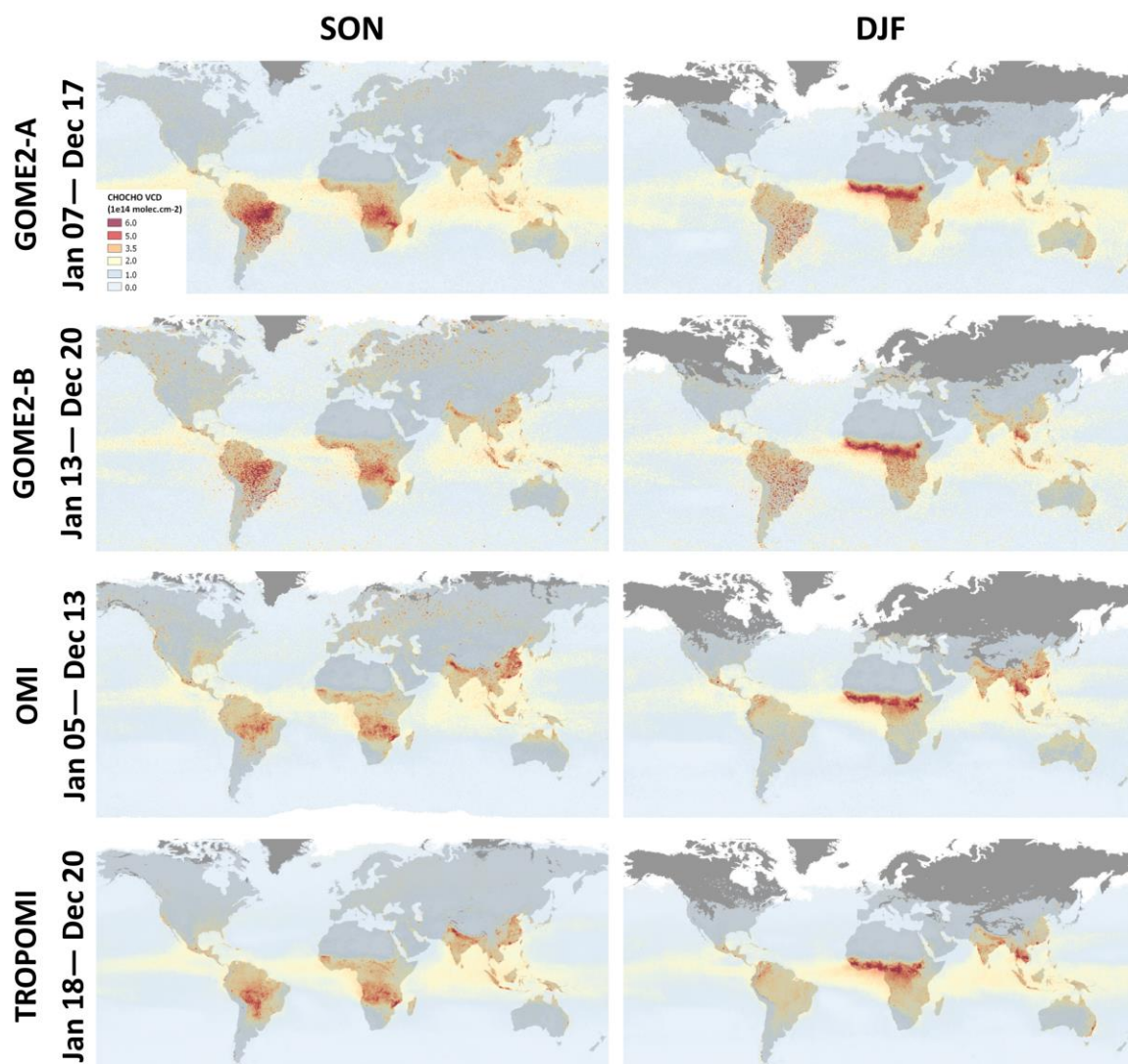


Figure 10: Comparison of long-term averaged global CHOCHO VCDs (in  $10^{14}$  molec/cm<sup>2</sup>) derived from GOME-2A, GOME-2B, OMI and TROPOMI sensors, for the March-April-May period (left panels) and the June-July-August period (right panels).





**Figure 11: Comparison of long-term averaged global CHOCHO VCDs (in  $10^{14}$  molec/cm<sup>2</sup>) derived from GOME-2A, GOME-2B, OMI and TROPOMI sensors, for the September-October-November period (left panels) and the December-January-February period (right panels).**

For a more detailed investigation of the consistency of the TROPOMI data set with OMI and GOME-2A/B, we compare complete time-series of monthly median glyoxal columns in selected regions (shown in Figure 12). The red rectangles indicate the regions on which we focus in Figure 13 and Figure 14, while the global statistics for all highlighted regions are given in Figure 15. Detailed figures are provided for all regions as supplementary material (Figures S1, S2, S3, S4). Figure 13 compares directly the four full time series, while Figure 14 compares the typical climatological seasonal variations as obtained by combining all available years. The error bars in the latter figure represent the interannual variability, and the 2-sigma standard deviation of the four satellite products is indicated as inset.

In the Tropics (e.g. Amazonia, Equatorial/North Central Africa), the four data sets are relatively stable over time. All instruments observe similar seasonal cycles and column values, although OMI appears to be slightly lower

than the others, in particular in Equatorial Africa. The inter-annual variability in Amazonia is high compared to other regions worldwide. Glyoxal is produced in that region to a large extent by fire emissions, which are highly variable. There is a direct correlation between years with high glyoxal columns and large fire emissions (e.g. 2007, 2010, 2015, 2019) as derived from the GFED database (van Der Werf et al., 2017; <https://www.globalfiredata.org/>). Interestingly, glyoxal columns measured by the morning GOME-2 instruments are larger than the OMI columns in the early afternoon during the fire seasons. This is consistent with the diurnal variation measured in satellite HCHO columns by De Smedt et al. (2015) and would deserve further investigation. Other regions display a more regular seasonal cycle, consistently seen by the four instruments.

In Asia, there are many hot spots, of which the origin is manifolds and strongly depends on the region and season. In addition to biogenic activities, large emissions due to fires may significantly contribute to the glyoxal columns. As illustrated in Figure 14, in the Indo-Gangetic Plain, there are typically two fire seasons in April/May and in October/November (after the Monsoon period) related to agricultural burning of wheat residue (Kumar et al., 2016), and leading to two maxima in the glyoxal VCD seasonal cycle with a significant interannual variability. For example, during the COVID-19 Indian lockdown in April/May 2020, fire activity has been reduced leading to smaller emissions (Levelt et al., 2021). This region is also highly populated, causing large emissions due to human activities. This is also true in North-East China where glyoxal columns remain significant in winter, while biogenic emissions are low during that period of the year. Although less variable than fire emissions, anthropogenic emissions may also change over time. Despite those variable emissions, the four data sets spanning different time periods show a high level of consistency. In China, it seems that the glyoxal columns as observed by OMI, GOME-2A and B are slightly reduced after 2014. This would deserve further investigation. On the other hand, any interpretation based on long-series of OMI data must be treated carefully since the instrument suffers from an evolving row anomaly (Schenkeveld et al., 2017), which impacts the stability of the product and causes an increasing number of outliers, especially at mid-latitudes. For example, over the Indo-Gangetic Plain, the OMI columns deviate regularly from the other instruments after 2014. In general, remnants of noise are also visible in the GOME-2 time series, which show somewhat less smooth time series than TROPOMI.

At mid-latitudes, the lower sun elevation, especially during local wintertime, makes the retrievals more challenging. Nevertheless, a small maximum is consistently observed during the local summertime. During wintertime, TROPOMI columns appear slightly lower than those from the other satellites. As mentioned before, the stronger impact of the row anomaly at mid/high-latitudes leads to a larger number of outliers in the OMI data set and to a low bias in winter after 2013/2014.

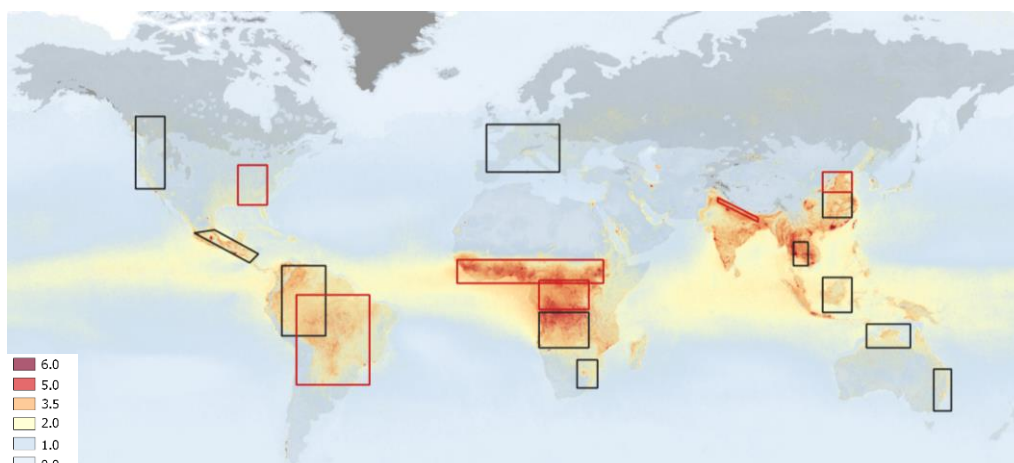


**Figure 12 : TROPOMI glyoxal VCD distribution (in  $1e14$  molec/cm<sup>2</sup>) averaged on the period January 2018-December 2020. The rectangles represent the regions where the glyoxal products from different satellites are intercompared with a specific focus on red regions in Figure 13 and Figure 14.**

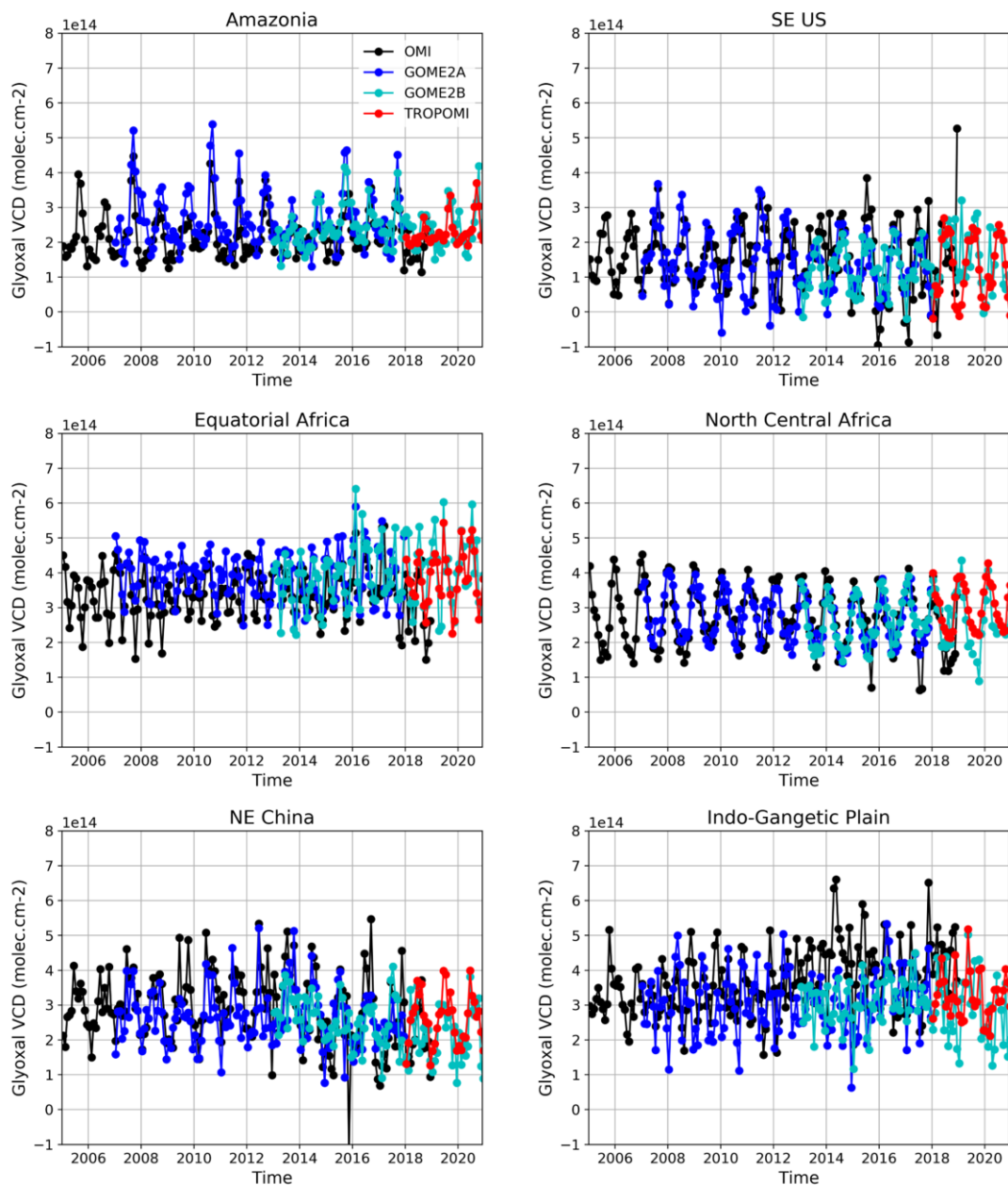


**Figure 13: Comparison of the monthly median glyoxal VCD time series from GOME-2A/B, OMI and TROPOMI in a few selected regions worldwide.**

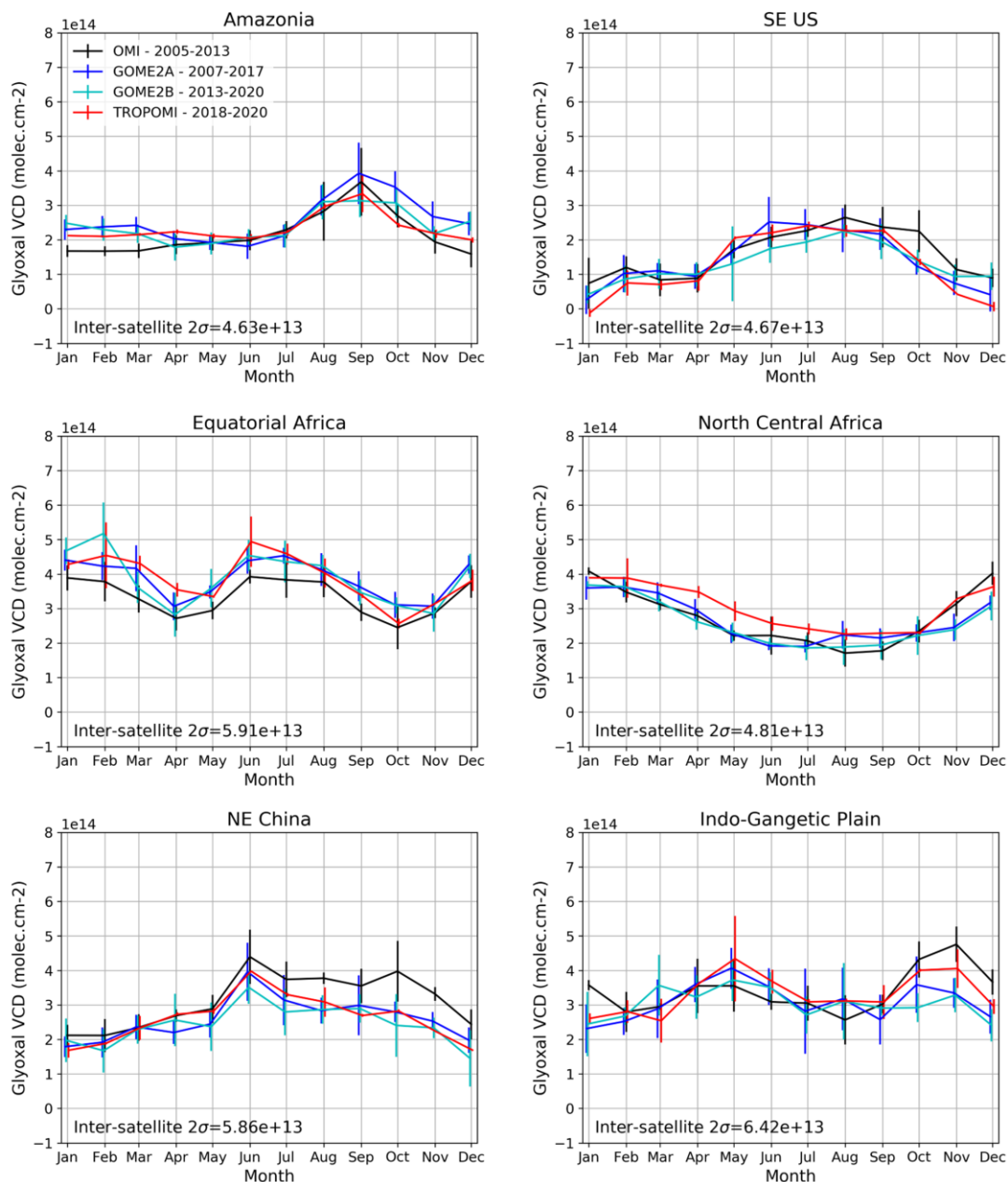


**Figure 14: Comparison of the climatological seasonal variation of the monthly median glyoxal VCDs from GOME-2A/B, OMI and TROPOMI in a few selected regions worldwide. The error bars represent the interannual variability as derived from the full time series.**

Figure 15 summarizes for all regions drawn in Figure 12 the absolute and relative deviation of each of the four data sets with respect to the median values of the ensemble. The symbols represent the median deviation considering all months of the year, while the error bars represent the full range of the monthly deviations. Regions are sorted by increasing mean glyoxal vertical column amounts and light and dark blue shaded areas indicate  $2.5 \times 10^{14}$  molec/cm<sup>2</sup> (50%) and  $1.5 \times 10^{14}$  molec/cm<sup>2</sup> (30%) differences as guidelines. Inter-satellite deviations are generally less than  $5 \times 10^{13}$  molec/cm<sup>2</sup> (20%). The large error bars in the relative differences plot for mid-latitude regions are caused by local wintertime months during which the glyoxal content is very low, if not negligible, and are therefore meaningless. Overall, the inter-satellite consistency of the glyoxal VCD products is excellent. In the [next](#) section



5, we will investigate the product quality with comparisons with independent ground-based MAX-DOAS glyoxal observations at a few stations in Asia and Europe.

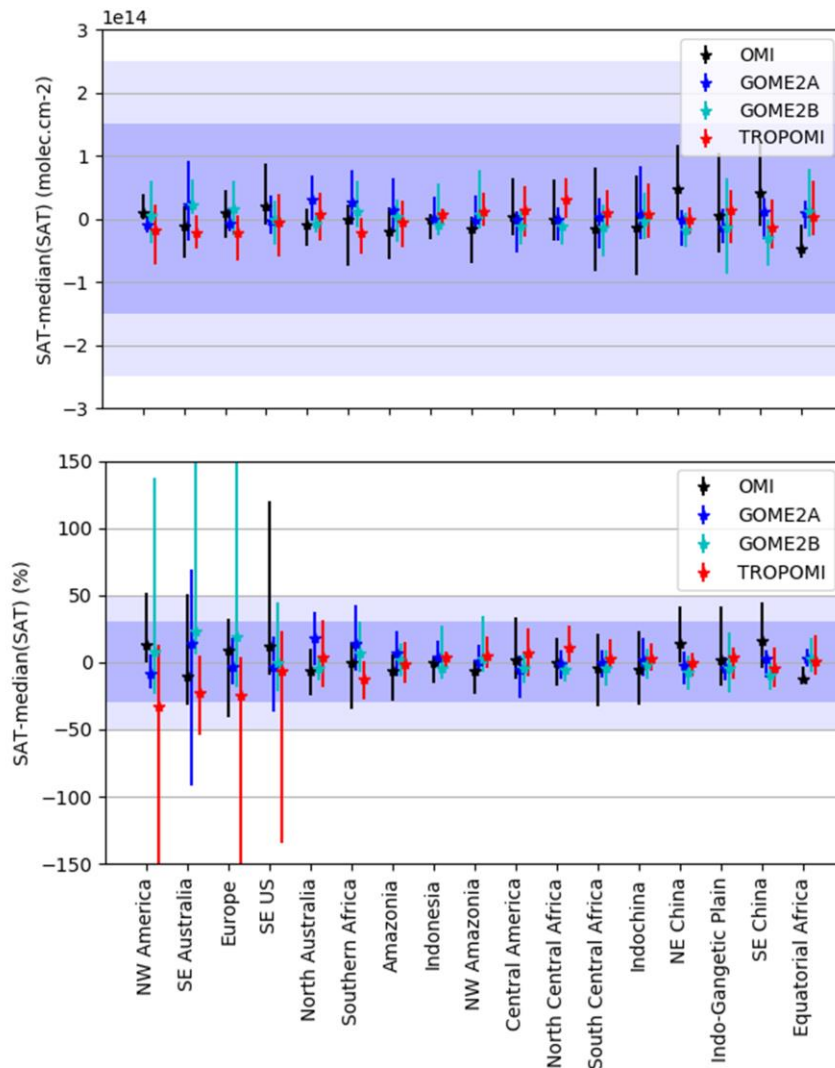


**Figure 15: Median deviation of the glyoxal VCD differences for TROPOMI, OMI, GOME-2A/B against the median value of the ensemble of the four data sets in the selected regions worldwide drawn in Figure 12. Those are plotted in absolute values (molec/cm<sup>2</sup>) in the upper panel and in relative values (%) in the lower panel. The error bars indicate the full range of the deviations considering climatological monthly data. Regions are sorted by increasing median glyoxal VCD value from left to right. The light and dark blue shaded area indicate differences of 1.5 molec/cm<sup>2</sup> (30%) and 2.5 molec/cm<sup>2</sup> (50%).**

#### 4.2.3. Glyoxal over equatorial oceans

A persistent equatorial oceanic glyoxal signal is seen consistently by the four sensors. The origin and the magnitude of the enhanced glyoxal concentrations over oceans remains nevertheless unclear. A similar feature has been observed from space in previous studies (Lerot et al., 2010; Vrekoussis et al., 2009; Wittrock et al.,

2006), while it was much less pronounced in others (Alvarado et al., 2014; Chan Miller et al., 2014). Over the past years, glyoxal measurements have been realized with ship-borne MAX-DOAS. While Sinreich et al. (2010) measured glyoxal concentrations up to 100 ppt in the marine boundary layer of the Equatorial Pacific Ocean, most other studies (Behrens et al., 2019b; Lawson et al., 2015; Mahajan et al., 2014; Volkamer et al., 2015) reported lower concentrations inconsistent with the satellite elevated glyoxal columns. However, Volkamer et al. (2015) also reported elevated glyoxal concentrations measured with an airborne MAX-DOAS in the free troposphere, which might explain the larger satellite glyoxal signal. Remaining spectral interferences may also contribute, at least partly, to this signal. In particular, its spatial correlation with high water vapour concentration regions and the high sensitivity of glyoxal retrievals to the water vapour cross-section as discussed in section 3.1 and by Chan Miller et al. (2014) call for a careful assessment of any future new data release or for future investigation on fit strategy to mitigate this interference (e.g. Kluge et al., 2020).

## **5. Validation with MAX-DOAS data**

### **5.1. Description of MAX-DOAS data sets and methodology**

MAX-DOAS instruments measure scattered solar light in the UV-Visible spectral range at different elevation angles above the horizon and allow retrieving information on trace gases and aerosol extinction in the altitude range below 2-3km of the atmosphere, where the instrumental sensitivity is the highest. In a first approximation, vertical columns of boundary layer gases can be estimated from MAX-DOAS measurements using a simple geometrical approach (Brinksma et al., 2008; Hönninger et al., 2004). More elaborated approaches exploit a set of different elevation angles to derive information on the vertical distribution of the gas concentration with up to 4 degrees of freedom, resulting in more accurate vertical columns in the 0-4 km altitude range (e.g. Beirle et al., 2019; Clémer et al., 2010; Irie et al., 2011; Friedrich et al., 2019).

Glyoxal concentrations can be derived from MAX-DOAS measurements in the visible range. However, the number of glyoxal MAX-DOAS data sets is very limited, especially those covering a period long enough to allow the validation of satellite data during entire seasonal cycles. Moreover, MAX-DOAS retrievals are affected by similar difficulties as satellite retrievals (noise, spectral interferences). Here, we collected an ensemble of data sets from nine stations located in Asia and Europe (see Table 3) spanning at least one year. Altogether a wide range of glyoxal columns and emission regimes are covered by those stations. Unfortunately, the approach to retrieve glyoxal from MAX-DOAS has not been homogenized so far, and they cannot be considered as true fiducial reference measurements. For example, although the same interfering species have been included in the DOAS fits, the reference cross-section data as well as the fitting interval may vary. The design (spectral range, spectral resolution, detector type, etc.) and operation mode of the instruments differ substantially, resulting in different sensitivities to changes in retrieval settings. Finally, the slant-to-vertical column conversion is performed differently from one station to another (see Table 3). Despite those limitations, the comparison of glyoxal tropospheric columns from satellites with nine different MAX-DOAS instruments is unprecedented.

Among the available MAX-DOAS data sets, three (Xianghe/China, Chiba/Japan and Phimai/Thailand) are long enough to allow a comparison with OMI and GOME-2A/B in addition to TROPOMI. The other ones span shorter,

and more recent periods and will be used only for comparison with the TROPOMI product. The Xianghe station has the longest and stable data record, and provide vertical profiles of glyoxal. Therefore we have used this reference station to perform a thorough analysis of the satellite product stability and of the impact of applying satellite averaging kernels. For the other stations, we performed a more qualitative comparison of the seasonal cycles of the glyoxal tropospheric columns. For the data colocation, we select MAX-DOAS data  $\pm 1.5$  hour around the satellite overpass time and satellite data within a radius of 100 km (150 km for Phimai) and 20 km around the station for GOME-2A/B/OMI and TROPOMI, respectively. Daily median glyoxal columns are computed if both satellite and ground-based data are available and finally monthly medians of the daily median columns are compared.

**Table 3 : List of MAX-DOAS stations used in the study and brief description of the approach to generate the glyoxal data.**

Station (coordinates) Time range	Institution PI	Retrieval Approach and fit interval	Reference
Xianghe/China (39.75°, 116.96°E) 2010-2020 Uccle/Belgium (50.78°N, 4.35°E) 2017-2020	BIRA-IASB	Profile retrieved using an Optimal Estimation scheme 436-468 nm	(Cl��mer et al., 2010; Hendrick et al., 2014)
Chiba/Japan (35.63°N, 140.10°E) 2012-2020 Phimai/Thailand (15.18°N, 140.10°E) 2014-2020 Pantnagar/India (29.03°N, 79.47°E) 2017-2020	CERES	Profile retrieved using a parametrization approach 436–457 nm	(Hoque et al., 2018; Irie et al., 2011)
Mohali/India (30.67°N, 76.73°E) May 2019 - 2020	MPIC/IISERM	Profile retrieved using a parametrization approach 400-460 nm	(Beirle et al., 2019; Kumar et al., 2020)
Athens/Greece (38.05°N, 23.80°E) 2018-2020 Vienna/Austria (48.18°N, 16.39°E) 2018-2020 Bremen/Germany (53.11°N, 8.86°E) 2018-2020	IUP-UB	Columns retrieved using the Geometrical Approximation 436-468 nm	(Alvarado et al., 2020b; Gratsea et al., 2016; Schreier et al., 2020)

## 5.2. Validation results

Figure 16 focuses on the comparison of monthly median glyoxal tropospheric columns retrieved from TROPOMI, OMI, GOME-2A and GOME-2B with columns from the BIRA-IASB MAX-DOAS instrument in Xianghe (China). The left panels compare the full time series for each satellite sensor with the MAX-DOAS data record. The right panels show the corresponding satellite/MAX-DOAS absolute differences. Note that the MAX-DOAS measurements have been interrupted from mid-2018 to mid-2019 due to an instrumental problem. Overall, all four

satellite instruments reproduce quite well the seasonal cycle seen by the MAX-DOAS instrument. However for all of them, except for the recent TROPOMI, a degradation appears after a few years of operation. For OMI, the consistency with the MAX-DOAS is ~~excellent~~ [satisfactory](#) before 2013, but the number of outliers increases afterwards and the columns during wintertime become too low. This is attributed to the evolving row anomaly as discussed in section 4.2. The GOME-2A/B data sets also agree quite well with the ground-based data for their first years of operation but then suffer from an increasing number of outliers after 2014 and 2017, respectively. Nonetheless, the quality of the data sets remains very reasonable. The ~~consistency of the~~ TROPOMI time series [also agrees well](#) with the MAX-DOAS ~~data is also excellent~~ and is characterized by a smooth temporal variability without any outliers on a monthly basis. The absolute differences shown in the right panels also clearly indicates a reduced scatter compared to the other satellites, despite the fact that a smaller overpass radius of 20 km was used instead of 100 km. This is reflected in the standard deviation of the differences given in the titles of each subpanels. The TROPOMI standard deviation is  $0.9 \times 10^{14}$  molec/cm<sup>2</sup>, while it is larger than  $1.7 \times 10^{14}$  molec/cm<sup>2</sup> for other sensors. On average, there are small negative biases with respect to the MAX-DOAS data for the four satellite time series (also given in the panel titles), ranging between  $-0.8 \times 10^{14}$  molec/cm<sup>2</sup> for TROPOMI and  $-1.5 \times 10^{14}$  molec/cm<sup>2</sup> for OMI. For this particular station, we investigated the impact of applying the satellite averaging kernels to smooth the MAX-DOAS glyoxal profiles. This process allows simulating MAX-DOAS columns which would be retrieved from the satellite algorithm, considering its own a priori profile information. The comparison of the satellite columns with the smoothed MAX-DOAS data therefore removes differences due to imperfect satellite a priori profile information. As shown in Figure 16, smoothing the MAX-DOAS columns reduces the satellite/MAX-DOAS bias to values ranging from  $-0.2 \times 10^{14}$  molec/cm<sup>2</sup> (TROPOMI) to  $-0.5 \times 10^{14}$  molec/cm<sup>2</sup> (OMI).

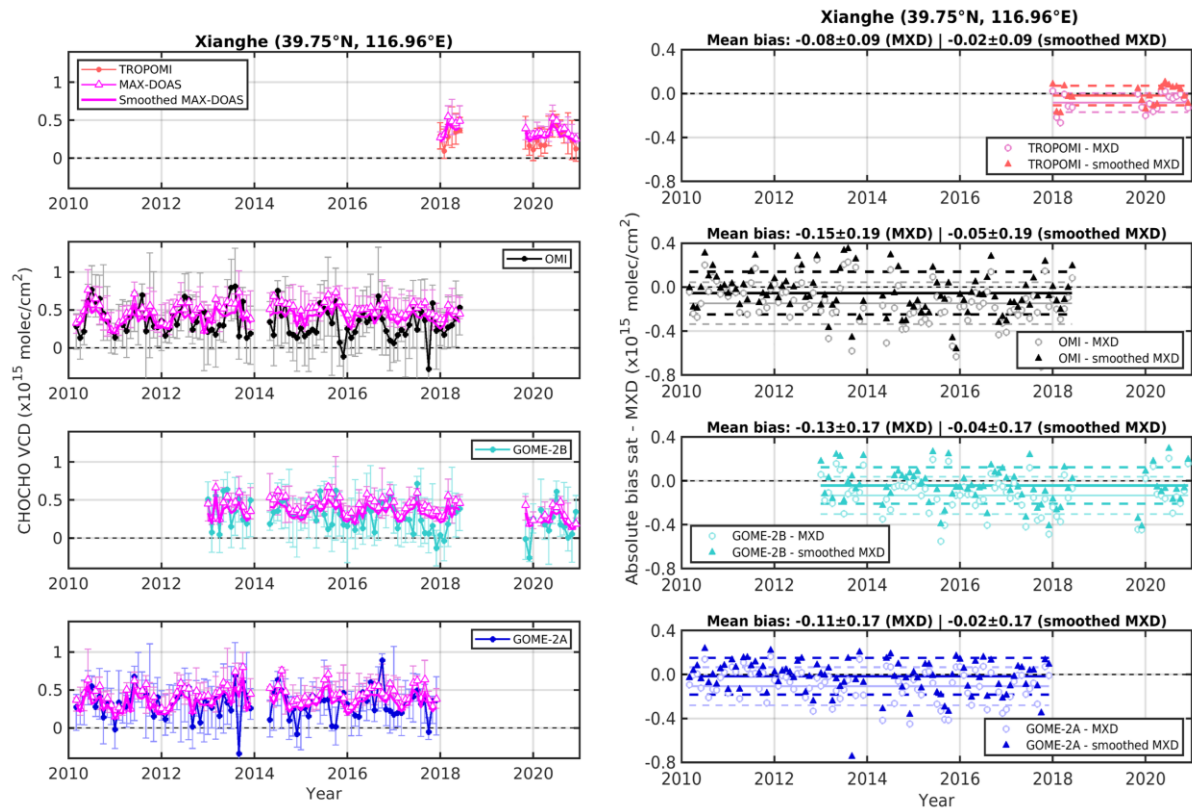


**Figure 16 : Comparison of the monthly median glyoxal tropospheric vertical columns retrieved from satellite and MAX-DOAS (MXD) instruments in Xianghe (China). The four left panels compare the time series from TROPOMI, OMI and GOME-2A/B with the MXD time series. MXD columns are also shown when smoothed with the satellite averaging kernels. The error bars represent the 25 and 75% percentiles. The four right panels show the corresponding time series of the satellite-MD absolute differences. Both original and smoothed MXD data are shown. Mean bias and standard deviation of the differences are given (in  $10^{15}$  molec/cm<sup>2</sup> units) in the panel titles and are also represented in the right panels with the full and dashed coloured lines.**

In Figure 17, we compare the median satellite and MAX-DOAS seasonal cycles of the glyoxal tropospheric columns at three stations (Xianghe, Chiba and Phimai) where the time series present a good overlap with the OMI and GOME-2A and B records, in addition to TROPOMI. In Xianghe, the seasonal cycle of the smoothed MAX-DOAS columns is also shown, illustrating again the reduction of the satellite/MAX-DOAS bias when the a priori profile error component is removed. Note that the OMI and GOME-2B seasonal cycles are computed using data until end of 2013 and 2016 to limit the impact of the increasing number of outliers. In each comparison panel, the MAX-DOAS cycle is always computed using the same time range as the satellite instrument. Overall, the seasonal patterns are consistently captured by the satellite and MAX-DOAS instruments. In Xianghe, the GOME-2A and TROPOMI cycles follow closely the MAX-DOAS curves, although TROPOMI slightly underestimates the MAX-DOAS columns during winter months. OMI and GOME-2B also reproduce the general seasonal pattern but show a somewhat more scattered curve, likely due to their slightly less stable time series. In Chiba where the glyoxal signal is mostly driven by biogenic emissions, the agreement between the satellites and the MAX-DOAS



measurements is excellent both in terms of variability and absolute values. Again, OMI shows a larger scatter (as also indicated by the larger error bars representing the inter-annual variability). In Phimai, where pyrogenic emissions are responsible for large glyoxal columns especially in the first few months of the year, the seasonal variability seen by the satellites and the MAX-DOAS is very consistent. A negative bias larger than for other stations is nevertheless observed. This can be related to other studies that identified larger biases in NO<sub>2</sub> or HCHO DOAS products for elevated column conditions (e.g. De Smedt et al., 2021; Verhoelst et al., 2021; Vigouroux et al., 2020). Possible causes for such biases are the different air masses probed by the satellite and ground-based instruments, their different vertical sensitivity as well as the a priori vertical profile information used in the retrieval algorithms.

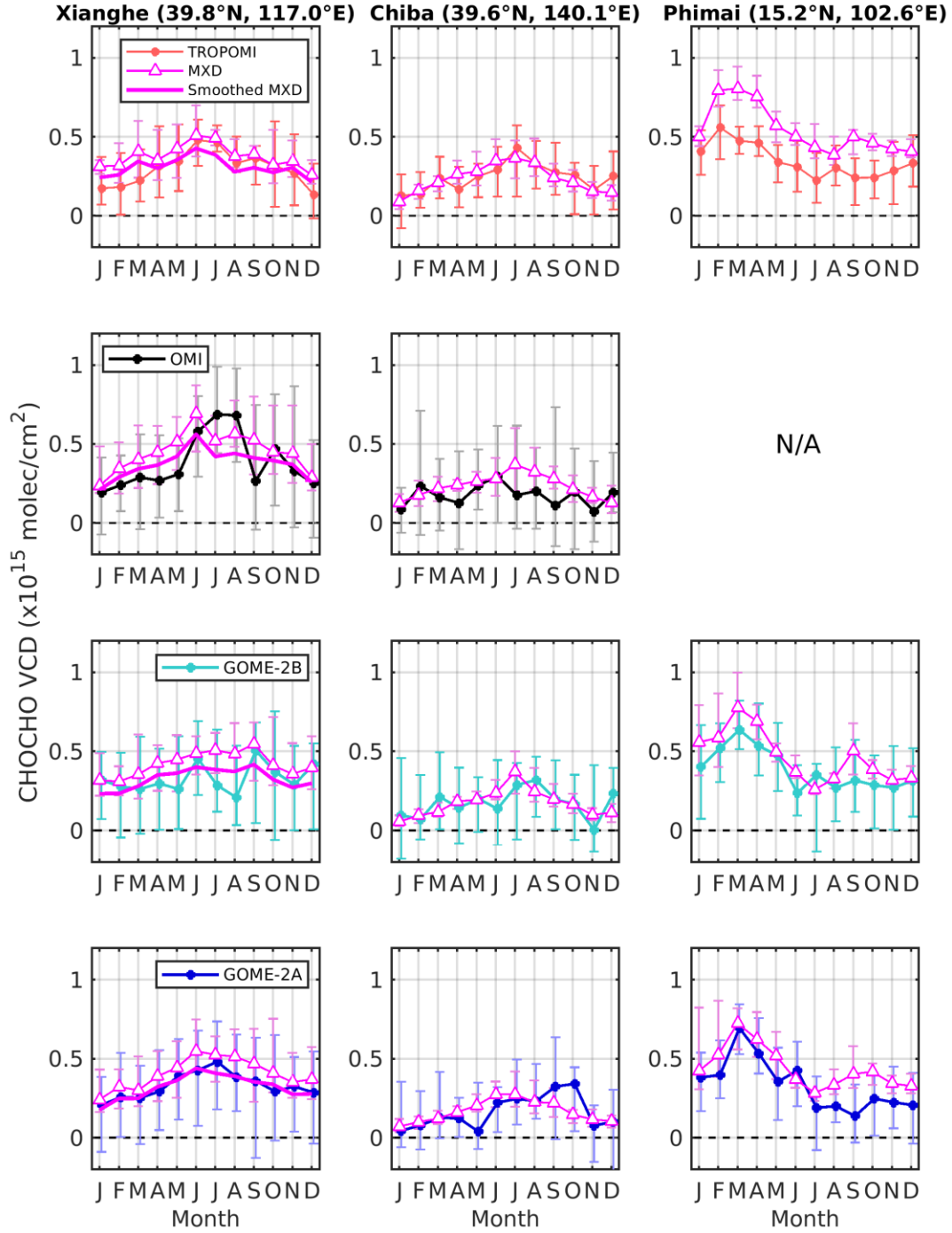
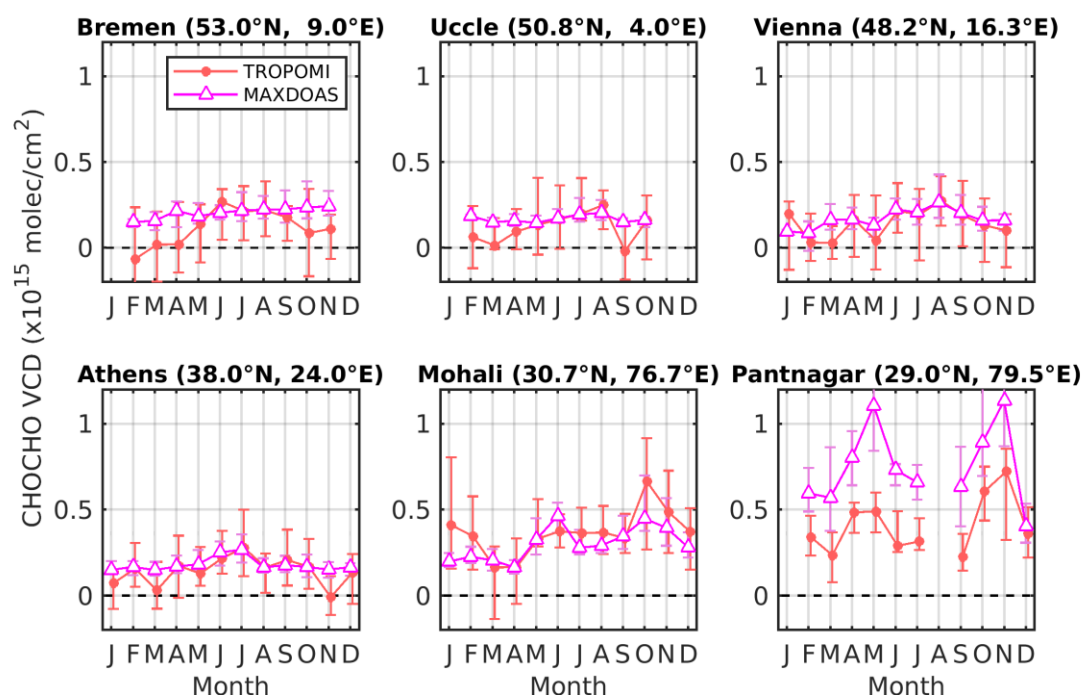


Figure 17 : Comparison of the monthly median glyoxal tropospheric vertical column seasonal cycle as retrieved from TROPOMI, OMI, GOME-2A/B and MXD in Xianghe (China), Chiba (Japan) and Phimai (Thailand). The columns correspond to the three stations and the rows to the different satellites. In Xianghe, MXD data smoothed with the satellite averaging kernels are also shown. The error bars represent the interannual variability (25% and 75% percentiles based on the full time series available). Note that the comparison of with the MAX-DOAS data in Phimai is not shown as the latter starts in 2014 when OMI is degraded.

818 In Figure 18, we compare again the seasonal cycle of glyoxal VCDs retrieved from TROPOMI with that from  
 819 more recent MAX-DOAS time series at six different stations. Four of them are located at mid-latitude in Europe  
 820 and show relatively low glyoxal columns, while larger average values are measured at the two other stations, in  
 821 Northern India (Mohali and Pantnagar). In Vienna/Austria and Athens/Greece, TROPOMI and MAX-DOAS  
 822 glyoxal columns agree very well and show consistent seasonal dependencies with maximum and minimum values  
 823 during summertime and wintertime, respectively. On the other hand, at the higher latitude stations of  
 824 Bremen/Germany and Uccle/Belgium, the consistency of the seasonal variations seen from space and from the  
 825 ground is somewhat poorer. While the glyoxal columns agree well during summertime, the satellite columns tend  
 826 to underestimate MAX-DOAS values in winter, the latter showing almost no seasonal variation. Satellite glyoxal  
 827 retrievals at those latitudes are challenging in winter because of the low sun elevation causing a reduced sensitivity  
 828 to the lowermost atmospheric layers. As mentioned in section 3.2, observations with solar zenith angles larger  
 829 than 70° are filtered for this reason, which explains the gap between November and January at those two stations.  
 830 In Uccle, we have also tested the impact of smoothing the MAX-DOAS columns with the satellite averaging  
 831 kernels (similarly as for Xianghe), which turned out to be very small. The absence of any seasonal dependence in  
 832 the cities of Brussels (Uccle) and Bremen, in contrast to that observed (although limited) in Vienna and Athens,  
 833 is to some extent puzzling. One should keep in mind however that the glyoxal retrievals from MAX-DOAS  
 834 measurements are also challenging and it cannot be excluded that errors in ground-based data might also partly  
 835 contribute to the observed differences.

836 In Mohali and Pantnagar, glyoxal columns are much larger and the seasonal variability is driven by fire emissions  
 837 and meteorological factors such as the monsoon. At those two stations, the glyoxal seasonal variability is very  
 838 well reproduced by TROPOMI. In terms of absolute values, the TROPOMI columns agree reasonably well in  
 839 Mohali but, they significantly underestimate the (large) MAX-DOAS columns in Pantnagar. The reason why the  
 840 systematic satellite/ground-based bias is so different between those two stations is unclear. MAX-DOAS columns  
 841 are clearly higher in Pantnagar than in Mohali pointing either to possible local differences in air quality, not  
 842 reflected in the satellite data, or to inconsistencies in the ground-based data sets. Although the agreement of the  
 843 absolute columns is reasonable ~~is excellent~~ in Mohali, the typical behaviour is an underestimation of the columns  
 844 by the satellites, as discussed before. Note also that those sites are significantly contaminated by aerosols, which  
 845 are neglected in the satellite retrievals (apart from the stringent cloud filtering). MAX-DOAS data have also been  
 846 analysed using very different approaches, which may also cause differences. This calls for a more detailed  
 847 analysis, which would require an homogenization of the MAX-DOAS data treatment, a more sophisticated  
 848 approach for the computation of the satellite AMFs (e.g. with an explicit aerosol treatment) and possibly some  
 849 independent information on the glyoxal vertical distribution. This being said, the nice consistency in the glyoxal  
 850 column seasonal variability by the different systems is remarkable in itself. Table 4 provides an overview of the  
 851 correlation coefficient between the satellite and the MAX-DOAS glyoxal columns at all considered stations. For  
 852 stations where the analysis was possible for all satellite sensors, the correlation coefficient was found to be  
 853 significantly better for TROPOMI than for the other instruments. It is also clear that correlation coefficients are  
 854 better for sites characterised by large and highly variable glyoxal columns (e.g. Asian stations). Apart from the  
 855 Bremen station where the negative bias during winter leads to a low correlation coefficient, all other values are  
 856 quite reasonable (between 0.61 and 0.87) for TROPOMI. Table 4 also gives the mean bias as derived from the

comparison of the satellite and MAX-DOAS glyoxal column seasonal cycle as well as the standard deviation of the differences. As discussed above, the mean differences are generally lower than  $1 \times 10^{14}$  molec/cm<sup>2</sup>, except for high columns where differences are noticeably higher.



**Figure 18 : Comparison of the monthly median glyoxal tropospheric vertical column seasonal cycle as retrieved from TROPOMI and MXD at four European stations (Bremen, Uccle, Vienna, Athens) and at two Indian stations (Mohali, Pantnagar). The error bars represent the interannual variability (25% and 75% percentiles based on the full time series available).**

**Table 4 : Correlation coefficients between the satellite and MAX-DOAS monthly median glyoxal tropospheric vertical columns as well as mean absolute difference and associated standard deviation at nine stations.**

	Correlation coefficient Mean bias $\pm$ standard deviation ( $\times 10^{14}$ molec/cm <sup>2</sup> )								
	Xianghe	Chiba	Phimai	Bremen	Uccle	Vienna	Athens	Mohali	Pantnagar
<b>TROPOMI</b>	0.87 -0.8 $\pm$ 0.6	0.80 0.1 $\pm$ 0.6	0.85 -2.0 $\pm$ 0.8	0.13 -0.9 $\pm$ 0.9	0.67 -0.5 $\pm$ 0.7	0.73 -0.3 $\pm$ 0.6	0.61 -0.4 $\pm$ 0.6	0.70 0.6 $\pm$ 0.9	0.78 -3.5 $\pm$ 1.5
<b>OMI (until 2013)</b>	0.70 -0.7 $\pm$ 1.3	0.32 -0.6 $\pm$ 0.8	N/A						

<b>GOME-2B (until 2016)</b>	0.37 -0.9±0.9	0.66 0.0±0.7	0.88 -0.8±0.8						
<b>GOME-2A</b>	0.92 -0.8±0.4	0.58 -0.1±0.9	0.86 -1.1±0.8						

## 6. Conclusions

We presented the first global TROPOMI glyoxal tropospheric column product derived from three years (2018-2020) of visible radiance measurements. The DOAS-based algorithm, which relies largely on previous developments for heritage satellite nadir-viewing instruments, has been further improved in different aspects. In particular, the use of additional pseudo cross-sections in the DOAS spectral fit allows mitigating the effect of the instrumental spectral response function perturbations in case of scene brightness inhomogeneity, which otherwise would lead to systematic biases in the retrieved glyoxal columns. This helps removing artefacts along the coasts and reducing pseudo-noise in regions covered by persistent broken clouds. The glyoxal slant columns are also empirically corrected for biases caused by the NO<sub>2</sub> misfit in case of strong absorption. Finally, the background correction procedure has been optimized for the TROPOMI characteristics and the a priori glyoxal vertical distribution, essential to the AMF computation, is now provided by the CTM MAGRITTE, an updated version of the IMAGES model, running at the higher spatial resolution of 1°x1°. The glyoxal column retrievals have been fully characterized with an error budget considering the different error components introduced in each of the algorithm modules. This allows extending the glyoxal column data product with total random and systematic error estimates provided for every observation, with corresponding averaging kernels and a priori profiles.

Glyoxal tropospheric columns have also been derived from data of the OMI, GOME-2A and GOME-2B satellite instruments using retrieval baselines similar to the TROPOMI algorithm. An extensive inter-comparison of those four data sets emphasised their excellent consistency with absolute mean glyoxal column differences found to be generally lower than  $0.5 \times 10^{14}$  molec/cm<sup>2</sup>. This demonstrates that glyoxal retrievals respond in the same manner to our selection of settings for all nadir-viewing satellite instruments. Because of this sensitivity, the retrievals may be easily impacted by spectral features caused by instrumental degradation. We have shown that the stability of the OMI and GOME-2 data records is somewhat degraded after a few years of operations. Glyoxal retrievals are characterized by a high level-of-noise, requiring significant spatio-temporal averaging to extract meaningful signals. With both a much larger number of observations and a finer spatial resolution, TROPOMI outperforms by far the previous instruments in its ability to provide high quality and detailed glyoxal fields. – Although consistently identified in our four satellite data sets, the origin of the glyoxal oceanic signal remains unclear. There appears to be an inconsistency between what is measured from space and most glyoxal concentration measurements conducted in marine boundary layer campaigns. Non-negligible glyoxal concentrations in the free troposphere as measured during one campaign (Volkamer et al., 2015) might reconcile the satellite and field data. On the other hand, part of this signal may also be partly caused by remaining spectral interferences (e.g. with water vapour).

Satellite observations have also been compared with a few independent MAX-DOAS data sets from stations located in Asia and Europe. Owing to the scarcity of MAX-DOAS glyoxal data sets, especially covering several



seasons, this validation exercise is therefore unprecedented. Based on a thorough analysis at the Xianghe station (China), where a 10-year time series of MAX-DOAS data is available, and on the comparison of seasonal cycles at other stations, we conclude that satellite and MAX-DOAS instruments observe consistent glyoxal signals and have similar intra-annual variations. This is reflected by the strong correlation coefficients, ranging between 0.61 and 0.87 for TROPOMI, with the exception of one mid-latitude station where the correlation is poorer. In general, the satellite and MAX-DOAS columns also agree in absolute values with differences less than  $1 \times 10^{14}$  molec/cm<sup>2</sup>, at least for stations with moderate columns. In Xianghe, we showed that the application of the satellite averaging kernels to the MAX-DOAS data further reduces the mean differences. There are however two stations (Phimai/Thailand and Pantnagar/India) where the satellite/MAX-DOAS bias is more significant, despite an excellent-reasonable agreement of the measured ~~between the~~ seasonal variations. Although ~~The~~ the origin of this bias is not fully understood, ~~the MAX-DOAS columns at those stations are very high and but~~ it is not uncommon to have such biases in UV-Visible satellite retrievals for strongly polluted sites. ~~It cannot be excluded that part of the bias originates from the MAX-DOAS retrieval strategy at those sites. In addition, w~~We have also indications that the satellite observations are low-biased during wintertime at mid-high latitudes where both the glyoxal signal is weak and the sensitivity to the boundary layer is reduced. The comparisons of OMI, GOME-2 and MAX-DOAS glyoxal columns also show reasonable agreement and similar intra-annual variability. Both the correlation coefficients and the scatter of the satellite/ground differences were however less good than those of TROPOMI. This points again to the better performance of TROPOMI for the detection of glyoxal from space and to its enhanced capability at providing information on VOC emissions. For future work, it would be beneficial to dedicate more efforts in the homogenization of the MAX-DOAS glyoxal retrievals in terms of both spectral analysis and slant-to-vertical column conversion in order to strengthen their potential for the validation of satellite data sets such as the one presented in this work.

## Data availability

Access to TROPOMI glyoxal tropospheric column data is possible via the GLYRETRO website (<https://glyretro.aeronomie.be/>), OMI glyoxal data can be obtained on request from the authors. Information to download the GOME-2/Metop-A and GOME-2/Metop-B glyoxal data records is provided at [https://acsaf.org/datarecord\\_access.php](https://acsaf.org/datarecord_access.php).

## Author contributions

CL is the main contributor to the study and led the writing of this paper. FH performed the validation exercise, with support from MVR and LMAA. MVR, LMAA, AR, IDS, NT, JV, HY and JVG contributed to algorithm and/or code development. TS and JFM provides the a priori modelled glyoxal profiles. PV and DL are responsible for the production of the GOME-2 glyoxal operational data records. MVR, FH, LMAA, SFS, HI, VK, TW, VS, TiW and PW contributed to operating the MAX-DOAS instruments, and to producing and providing glyoxal data. CR supervised the study. All co-authors have been involved into the discussion of results and the writing of this article.

## Competing interests

The authors have the following competing interests: Thomas Wagner is chief-executive editor of AMT. Andreas Richter is executive editor of AMT. Diego Loyola, Andreas Richter, Michel Van Roozendaal and Thomas

Wagner act as associate editors for AMT.

## Acknowledgments

This work contains modified Copernicus Sentinel-5 Precursor satellite data (2018-2020). It has been supported by the European Space Agency via the preparation of the Level-2 Prototype Processor of the future Copernicus Sentinel-5 satellite (contract #4000118463/16/NL/AI) and via the GLYRETRO project, part of the Sentinel-5p+Innovation programme (contract #4000127610/19/I-NS). EUMETSAT, the Belgian Federal Science Policy Office (BELSPO) and the German Aerospace Center (DLR) are acknowledged for their respective financial support of the GOME-2 algorithmic developments through the AC SAF Continuous Development and Operations Phase (CDOP-3) and the ProDEx B-ACSAF contribution to the ACSAF. The Vienna MAX-DOAS instrument is part of the VINDOBONA project, which is funded by the Austrian Science Fund (FWF): I 2296-N29, the German Science Foundation (DFG): Ri1800/6-1, and A1 Telekom Austria. IISER Mohali Atmospheric Chemistry Facility is gratefully acknowledged for supporting the MAX-DOAS operations in Mohali, India. We thank Caroline Fayt and Christian Herman from BIRA-IASB for maintaining the Uccle and Xianghe MAX-DOAS instruments.

## References

- Abbot, D. S., Palmer, P. I., Martin, R. V., Chance, K. V., Jacob, D. J. and Guenther, A.: Seasonal and interannual variability of North American isoprene emissions as determined by formaldehyde column measurements from space, *Geophys. Res. Lett.*, 30(17), n/a-n/a, doi:10.1029/2003GL017336, 2003.
- Aliwell, S. R., Van Roozendaal, M., Johnston, P. V., Richter, A., Wagner, T., Arlander, D. W., Burrows, J. P., Fish, D. J., Jones, R. L., Tørnkvist, K. K., Lambert, J. C., Pfeilsticker, K. and Pundt, I.: Analysis for BrO in zenith-sky spectra: An intercomparison exercise for analysis improvement, *J. Geophys. Res. Atmos.*, 107(14), ACH 10-1, doi:10.1029/2001JD000329, 2002.
- Alvarado, L. M. A., Richter, A., Vrekoussis, M., Wittrock, F., Hilboll, A., Schreier, S. F. and Burrows, J. P.: An improved glyoxal retrieval from OMI measurements, *Atmos. Meas. Tech.*, 7(12), 4133–4150, doi:10.5194/amt-7-4133-2014, 2014.
- Alvarado, L. M. A., Richter, A., Vrekoussis, M., Hilboll, A., Kalisz Hedegaard, A. B., Schneising, O. and Burrows, J. P.: Unexpected long-range transport of glyoxal and formaldehyde observed from the Copernicus Sentinel-5 Precursor satellite during the 2018 Canadian wildfires, *Atmos. Chem. Phys.*, 20(4), 2057–2072, doi:10.5194/acp-20-2057-2020, 2020.
- Azam, F. and Richter, A.: GOME2 on MetOp Follow-on analysis of GOME2 in orbit degradation Final Report, 2015.
- Barkley, M. P., Smedt, I. De, Van Roozendaal, M., Kurosu, T. P., Chance, K., Arneth, A., Hagberg, D., Guenther, A., Paulot, F., Marais, E. and Mao, J.: Top-down isoprene emissions over tropical South America inferred from SCIAMACHY and OMI formaldehyde columns, *J. Geophys. Res. Atmos.*, 118(12), 6849–6868, doi:10.1002/jgrd.50552, 2013.

975 Barkley, M. P., González Abad, G., Kurosu, T. P., Spurr, R., Torbatian, S. and Lerot, C.: OMI air-quality  
 976 monitoring over the Middle East, *Atmos. Chem. Phys.*, 17, 4687–4709, doi:10.5194/acp-17-4687-2017, 2017.

977 Bauwens, M., Stavrakou, T., Müller, J.-F., De Smedt, I., Van Roozendaal, M., van der Werf, G. R.,  
 978 Wiedinmyer, C., Kaiser, J. W., Sindelarova, K. and Guenther, A.: Nine years of global hydrocarbon emissions  
 979 based on source inversion of OMI formaldehyde observations, *Atmos. Chem. Phys.*, 16(15), 10133–10158,  
 980 doi:10.5194/acp-16-10133-2016, 2016.

981 Beekmann, M. and Vautard, R.: A modelling study of photochemical regimes over Europe: robustness and  
 982 variability, *Atmos. Chem. Phys.*, 10(20), 10067–10084, doi:10.5194/acp-10-10067-2010, 2010.

983 Behrens, L. K., Hilboll, A., Richter, A., Peters, E., Alvarado, L. M. A., Kalisz Hedegaard, A. B., Wittrock, F.,  
 984 Burrows, J. P. and Vrekoussis, M.: Detection of outflow of formaldehyde and glyoxal from the African  
 985 continent to the Atlantic Ocean with a MAX-DOAS instrument, *Atmos. Chem. Phys.*, 19(15), 10257–10278,  
 986 doi:10.5194/acp-19-10257-2019, 2019a.

987 Behrens, L. K., Hilboll, A., Richter, A., Peters, E., Alvarado, L. M. A., Hedegaard, A. B. K., Wittrock, F.,  
 988 Burrows, J. P. and Vrekoussis, M.: Detection of outflow of formaldehyde and glyoxal from the African  
 989 continent to the Atlantic Ocean with a MAX-DOAS instrument, *Atmos. Chem. Phys.*, 19(15), 10257–10278,  
 990 doi:10.5194/acp-19-10257-2019, 2019b.

991 Beirle, S., Dörner, S., Donner, S., Remmers, J., Wang, Y. and Wagner, T.: The Mainz profile algorithm  
 992 (MAPA), *Atmos. Meas. Tech.*, 12(3), 1785–1806, doi:10.5194/amt-12-1785-2019, 2019.

993 Benavent, N., Garcia-Nieto, D., Wang, S. and Saiz-Lopez, A.: MAX-DOAS measurements and vertical profiles  
 994 of glyoxal and formaldehyde in Madrid, Spain, *Atmos. Environ.*, 199, 357–367,  
 995 doi:10.1016/j.atmosenv.2018.11.047, 2019.

996 Boersma, K. F., Eskes, H. J., Veefkind, J. P., Brinksma, E. J., Van Der A, R. J., Sneep, M., Van Den Oord, G.  
 997 H. J., Levelt, P. F., Stammes, P., Gleason, J. F. and Bucsela, E. J.: Near-real time retrieval of tropospheric NO<sub>2</sub>  
 998 from OMI, *Atmos. Chem. Phys.*, 7(8), 2103–2118, doi:10.5194/acp-7-2103-2007, 2007.

999 Boersma, K. F., Eskes, H. J., Dirksen, R. J., van der A, R. J., Veefkind, J. P., Stammes, P., Huijnen, V.,  
 1000 Kleipool, Q. L., Sneep, M., Claas, J., Leitão, J., Richter, A., Zhou, Y. and Brunner, D.: An improved  
 1001 tropospheric NO<sub>2</sub> column retrieval algorithm for the Ozone Monitoring Instrument, *Atmos. Meas. Tech.*, 4(9),  
 1002 1905–1928, doi:10.5194/amt-4-1905-2011, 2011.

1003 Brinksma, E. J., Pinardi, G., Volten, H., Braak, R., Richter, A., Schönhardt, A., van Roozendaal, M., Fayt, C.,  
 1004 Hermans, C., Dirksen, R. J., Vlemmix, T., Berkhout, A. J. C., Swart, D. P. J., Oetjen, H., Wittrock, F., Wagner,  
 1005 T., Ibrahim, O. W., de Leeuw, G., Moerman, M., Curier, R. L., Celarier, E. A., Cede, A., Knap, W. H.,  
 1006 Veefkind, J. P., Eskes, H. J., Allaart, M., Rothe, R., Piter, A. J. M. and Levelt, P. F.: The 2005 and 2006  
 1007 DANDELIONS NO<sub>2</sub> and aerosol intercomparison campaigns, *J. Geophys. Res.*, 113(D16), D16S46,  
 1008 doi:10.1029/2007JD008808, 2008.

1009 Cao, H., Fu, T. M., Zhang, L., Henze, D. K., Miller, C. C., Lerot, C., Abad, G. G., De Smedt, I., Zhang, Q., Van  
 1010 Roozendaal, M., Hendrick, F., Chance, K., Li, J., Zheng, J. and Zhao, Y.: Adjoint inversion of Chinese non-

methane volatile organic compound emissions using space-based observations of formaldehyde and glyoxal, Atmos. Chem. Phys., 18(20), 15017–15046, doi:10.5194/acp-18-15017-2018, 2018.

Chan, A. W. H., Chan, M. N., Surratt, J. D., Chhabra, P. S., Loza, C. L., Crounse, J. D., Yee, L. D., Flagan, R. C., Wennberg, P. O. and Seinfeld, J. H.: Role of aldehyde chemistry and NO<sub>x</sub> concentrations in secondary organic aerosol formation, Atmos. Chem. Phys. Discuss., 10(4), 10219–10269 [online] Available from: <http://www.atmos-chem-phys-discuss.net/10/10219/2010/>, 2010.

Chan Miller, C., Gonzalez Abad, G., Wang, H., Liu, X., Kurosu, T., Jacob, D. J. and Chance, K.: Glyoxal retrieval from the Ozone Monitoring Instrument, Atmos. Meas. Tech., 7(11), 3891–3907, doi:10.5194/amt-7-3891-2014, 2014.

Chan Miller, C., Jacob, D. J., Marais, E. A., Yu, K., Travis, K. R., Kim, P. S., Fisher, J. A., Zhu, L., Wolfe, G. M., Hanisco, T. F., Keutsch, F. N., Kaiser, J., Min, K.-E., Brown, S. S., Washenfelder, R. A., González Abad, G. and Chance, K.: Glyoxal yield from isoprene oxidation and relation to formaldehyde: chemical mechanism, constraints from SENEX aircraft observations, and interpretation of OMI satellite data, Atmos. Chem. Phys., 17(14), 8725–8738, doi:10.5194/acp-17-8725-2017, 2017.

Chance, K. and Kurucz, R. L.: An improved high-resolution solar reference spectrum for earth's atmosphere measurements in the ultraviolet, visible, and near infrared, J. Quant. Spectrosc. Radiat. Transf., 111(9), 1289–1295, doi:10.1016/j.jqsrt.2010.01.036, 2010.

Chance, K. V. and Spurr, R. J. D.: Ring effect studies: Rayleigh scattering, including molecular parameters for rotational Raman scattering, and the Fraunhofer spectrum, Appl. Opt., 36(21), 5224, doi:10.1364/ao.36.005224, 1997.

Clémer, K., Van Roozendaal, M., Fayt, C., Hendrick, F., Hermans, C., Pinardi, G., Spurr, R., Wang, P. and De Mazière, M.: Multiple wavelength retrieval of tropospheric aerosol optical properties from MAXDOAS measurements in Beijing, Atmos. Meas. Tech., 3(4), 863–878, doi:10.5194/amt-3-863-2010, 2010.

Coburn, S., Ortega, I., Thalman, R., Blomquist, B., Fairall, C. W. and Volkamer, R.: Measurements of diurnal variations and eddy covariance (EC) fluxes of glyoxal in the tropical marine boundary layer: description of the Fast LED-CE-DOAS instrument, Atmos. Meas. Tech. Discuss., 7(10), 6245–6285, doi:10.5194/amt-7-3579-2014, 2014.

Curci, G., Palmer, P. I., Kurosu, T. P., Chance, K. and Visconti, G.: Estimating European volatile organic compound emissions using satellite observations of formaldehyde from the Ozone Monitoring Instrument, Atmos. Chem. Phys., 10(23), 11501–11517, doi:10.5194/acp-10-11501-2010, 2010.

Danckaert, T., Fayt, C., van Roozendaal, M., De Smedt, I., Letocard, V., Merlaud, A. and Pinardi, G.: QDOAS software user manual. [online] Available from: [http://uv-vis.aeronomie.be/software/QDOAS/QDOAS\\_manual.pdf](http://uv-vis.aeronomie.be/software/QDOAS/QDOAS_manual.pdf), 2017.

Danielson, J. J. and Gesch, D. B.: Global multi-resolution terrain elevation data 2010 (GMTED2010), 2011.

De Smedt, I., Müller, J.-F., Stavrou, T., van der A, R., Eskes, H. and Van Roozendaal, M.: Twelve years of

1046 global observations of formaldehyde in the troposphere using GOME and SCIAMACHY sensors, *Atmos.*  
 1047 *Chem. Phys.*, 8(16), 4947–4963 [online] Available from: <http://www.atmos-chem-phys.net/8/4947/2008/>, 2008.

1048 De Smedt, I., Stavrakou, T., Hendrick, F., Danckaert, T., Vlemmix, T., Pinardi, G., Theys, N., Lerot, C., Gielen,  
 1049 C., Vigouroux, C., Hermans, C., Fayt, C., Veefkind, P., Müller, J.-F. and Van Roozendaal, M.: Diurnal, seasonal  
 1050 and long-term variations of global formaldehyde columns inferred from combined OMI and GOME-2  
 1051 observations, *Atmos. Chem. Phys.*, 15(21), 12519–12545, doi:10.5194/acp-15-12519-2015, 2015.

1052 De Smedt, I., Theys, N., Yu, H., Danckaert, T., Lerot, C., Compernelle, S., Van Roozendaal, M., Richter, A.,  
 1053 Hilboll, A., Peters, E., Pedernana, M., Loyola, D., Beirle, S., Wagner, T., Eskes, H., van Geffen, J., Boersma,  
 1054 K. F. and Veefkind, P.: Algorithm theoretical baseline for formaldehyde retrievals from S5P TROPOMI and  
 1055 from the QA4ECV project, *Atmos. Meas. Tech.*, 11(4), 2395–2426, doi:10.5194/amt-11-2395-2018, 2018.

1056 De Smedt, I., Pinardi, G., Vigouroux, C., Compernelle, S., Bais, A., Benavent, N., Boersma, F., Chan, K.-L.,  
 1057 Donner, S., Eichmann, K.-U., Hedelt, P., Hendrick, F., Irie, H., Kumar, V., Lambert, J.-C., Langerock, B., Lerot,  
 1058 C., Liu, C., Loyola, D., Piders, A., Richter, A., Rivera Cárdenas, C., Romahn, F., Ryan, R. G., Sinha, V., Theys,  
 1059 N., Vlietinck, J., Wagner, T., Wang, T., Yu, H. and Van Roozendaal, M.: Comparative assessment of  
 1060 TROPOMI and OMI formaldehyde observations and validation against MAX-DOAS network column  
 1061 measurements, *Atmos. Chem. Phys.*, 21(16), 12561–12593, doi:10.5194/ACP-21-12561-2021, 2021.

1062 DiGangi, J. P., Henry, S. B., Kammrath, A., Boyle, E. S., Kaser, L., Schnitzhofer, R., Graus, M., Turnipseed,  
 1063 A., Weber, R. J., Hornbrook, R. S., Cantrell, C. A., Maudlin, R. L., Kim, S., Nakashima, Y., Wolfe, G. M.,  
 1064 Kajii, Y., Apel, E. C. C., Goldstein, A. H., Guenther, A., Karl, T., Hansel, A., Keutsch, F. N., Park, J.-H. J.-H.,  
 1065 Weber, R. J., Hornbrook, R. S., Cantrell, C. A., Maudlin III, R. L., Kim, S., Nakashima, Y., Wolfe, G. M., Kajii,  
 1066 Y., Apel, E. C. C., Goldstein, A. H., Guenther, A., Karl, T., Hansel, A. and Keutsch, F. N.: Observations of  
 1067 glyoxal and formaldehyde as metrics for the anthropogenic impact on rural photochemistry, *Atmos. Chem.*  
 1068 *Phys.*, 12(20), 9529–9543, doi:10.5194/acp-12-9529-2012, 2012.

1069 Eskes, H. J. and Boersma, K. F.: Averaging kernels for DOAS total-column satellite retrievals, *Atmos. Chem.*  
 1070 *Phys.*, 3(5), 1285–1291, doi:10.5194/acp-3-1285-2003, 2003.

1071 EUMETSAT: GOME-2 Product Guide (EUM/OPS-EPS/MAN/07/0445), (March) [online] Available from:  
 1072 <http://www.eumetsat.int>, 2011.

1073 Fu, T.-M. T.-M., Jacob, D. J., Wittrock, F., Burrows, J. P., Vrekoussis, M. and Henze, D. K.: Global budgets of  
 1074 atmospheric glyoxal and methylglyoxal, and implications for formation of secondary organic aerosols, *J.*  
 1075 *Geophys. Res.*, 113(D15), D15303, doi:10.1029/2007JD009505, 2008.

1076 van Geffen, J. H. G. M., Eskes, H. J., Boersma, K. F., Maasackers, J. D. and Veefkind, J. P.: TROPOMI ATBD  
 1077 of the total and tropospheric NO<sub>2</sub> data products, S5p/TROPOMI, (1.4.0), 1–76 [online] Available from:  
 1078 <https://sentinel.esa.int/documents/247904/2476257/Sentinel-5P-TROPOMI-ATBD-NO2-data-products>, 2019.

1079 Gordon, I. E., Rothman, L. S., Hill, C., Kochanov, R. V., Tan, Y., Bernath, P. F., Birk, M., Boudon, V.,  
 1080 Campargue, A., Chance, K. V., Drouin, B. J., Flaud, J. M., Gamache, R. R., Hodges, J. T., Jacquemart, D.,  
 1081 Perevalov, V. I., Perrin, A., Shine, K. P., Smith, M. A. H., Tennyson, J., Toon, G. C., Tran, H., Tyuterev, V. G.,



1082 Barbe, A., Császár, A. G., Devi, V. M., Furtenbacher, T., Harrison, J. J., Hartmann, J. M., Jolly, A., Johnson, T.  
1083 J., Karman, T., Kleiner, I., Kyuberis, A. A., Loos, J., Lyulin, O. M., Massie, S. T., Mikhailenko, S. N.,  
1084 Moazzen-Ahmadi, N., Müller, H. S. P., Naumenko, O. V., Nikitin, A. V., Polyansky, O. L., Rey, M., Rotger,  
1085 M., Sharpe, S. W., Sung, K., Starikova, E., Tashkun, S. A., Auwera, J. Vander, Wagner, G., Wilzewski, J.,  
1086 Weislo, P., Yu, S. and Zak, E. J.: The HITRAN2016 molecular spectroscopic database, *J. Quant. Spectrosc.*  
1087 *Radiat. Transf.*, 203, 3–69, doi:10.1016/j.jqsrt.2017.06.038, 2017.

1088 Gratsea, M., Vrekoussis, M., Richter, A., Wittrock, F., Schönhardt, A., Burrows, J., Kazadzis, S., Mihalopoulos,  
1089 N. and Gerasopoulos, E.: Slant column MAX-DOAS measurements of nitrogen dioxide, formaldehyde, glyoxal  
1090 and oxygen dimer in the urban environment of Athens, *Atmos. Environ.*, 135, 118–131,  
1091 doi:10.1016/J.ATMOSENV.2016.03.048, 2016.

1092 Guenther, A. B., Jiang, X., Heald, C. L., Sakulyanontvittaya, T., Duhl, T., Emmons, L. K. and Wang, X.: The  
1093 Model of Emissions of Gases and Aerosols from Nature version 2.1 (MEGAN2.1): an extended and updated  
1094 framework for modeling biogenic emissions, *Geosci. Model Dev.*, 5(6), 1471–1492, doi:10.5194/gmd-5-1471-  
1095 2012, 2012.

1096 Hallquist, M., Wenger, J. C., Baltensperger, U., Rudich, Y., Simpson, D., Claeys, M., Dommen, J., Donahue, N.  
1097 M., George, C., Goldstein, A. H., Hamilton, J. F., Herrmann, H., Hoffmann, T., Iinuma, Y., Jang, M., Jenkin, M.  
1098 E., Jimenez, J. L., Kiendler-Scharr, A., Maenhaut, W., McFiggans, G., Mentel, T. F., Monod, A., Prévôt, A. S.  
1099 H., Seinfeld, J. H., Surratt, J. D., Szmigielski, R. and Wildt, J.: The formation, properties and impact of  
1100 secondary organic aerosol: current and emerging issues, *Atmos. Chem. Phys.*, 9(14), 5155–5236 [online]  
1101 Available from: <http://www.atmos-chem-phys.net/9/5155/2009/>, 2009.

1102 Hendrick, F., Clémer, K., Wang, P., De Mazière, M., Fayt, C., Gielen, C., Hermans, C., Ma, J. Z., Pinardi, G.,  
1103 Stavrakou, T., Vlemmix, T. and Van Roozendaal, M.: Four years of ground-based MAX-DOAS observations of  
1104 HONO and NO<sub>2</sub> in the Beijing area, *Atmos. Chem. Phys.*, 14(2), 765–781, doi:10.5194/acp-14-765-2014, 2014.

1105 Hönninger, G., von Friedeburg, C. and Platt, U.: Multi axis differential optical absorption spectroscopy (MAX-  
1106 DOAS), *Atmos. Chem. Phys.*, 4(1), 231–254, doi:10.5194/acp-4-231-2004, 2004.

1107 Hoque, H. M. S., Irie, H. and Damiani, A.: First MAX-DOAS Observations of Formaldehyde and Glyoxal in  
1108 Phimai, Thailand, *J. Geophys. Res. Atmos.*, 123(17), 9957–9975, doi:10.1029/2018JD028480, 2018.

1109 Huang, G., Brook, R., Crippa, M., Janssens-Maenhout, G., Schieberle, C., Dore, C., Guizzardi, D., Muntean,  
1110 M., Schaaf, E. and Friedrich, R.: Speciation of anthropogenic emissions of non-methane volatile organic  
1111 compounds: A global gridded data set for 1970–2012, *Atmos. Chem. Phys.*, 17(12), 7683–7701,  
1112 doi:10.5194/acp-17-7683-2017, 2017.

1113 Irie, H., Takashima, H., Kanaya, Y., Boersma, K. F., Gast, L., Wittrock, F., Brunner, D., Zhou, Y. and Van  
1114 Roozendaal, M.: Eight-component retrievals from ground-based MAX-DOAS observations, *Atmos. Meas.*  
1115 *Tech.*, 4(6), 1027–1044, doi:10.5194/amt-4-1027-2011, 2011.

1116 Jacob, D. J.: Introduction to Atmospheric Chemistry, Princeton University Press. [online] Available from:  
1117 <https://press.princeton.edu/books/hardcover/9780691001852/introduction-to-atmospheric-chemistry> (Accessed

1118 19 March 2021), 2000.

1119 Javed, Z., Liu, C., Khokhar, M., Tan, W., Liu, H., Xing, C., Ji, X., Tanvir, A., Hong, Q., Sandhu, O., Rehman,  
 1120 A., Javed, Z., Liu, C., Khokhar, M. F., Tan, W., Liu, H., Xing, C., Ji, X., Tanvir, A., Hong, Q., Sandhu, O. and  
 1121 Rehman, A.: Ground-Based MAX-DOAS Observations of CHOCHO and HCHO in Beijing and Baoding,  
 1122 China, *Remote Sens.*, 11(13), 1524, doi:10.3390/rs11131524, 2019.

1123 Jin, X., Jin, X., Fiore, A., Fiore, A., Boersma, K. F., Boersma, K. F., Smedt, I. De and Valin, L.: Inferring  
 1124 Changes in Summertime Surface Ozone-NO<sub>x</sub>-VOC Chemistry over U.S. Urban Areas from Two Decades of  
 1125 Satellite and Ground-Based Observations, *Environ. Sci. Technol.*, 54(11), 6518–6529,  
 1126 doi:10.1021/acs.est.9b07785, 2020.

1127 Kaiser, J., Wolfe, G. M., Min, K. E., Brown, S. S., Miller, C. C., Jacob, D. J., deGouw, J. A., Graus, M.,  
 1128 Hanisco, T. F., Holloway, J., Peischl, J., Pollack, I. B., Ryerson, T. B., Warneke, C., Washenfelder, R. A. and  
 1129 Keutsch, F. N.: Reassessing the ratio of glyoxal to formaldehyde as an indicator of hydrocarbon precursor  
 1130 speciation, *Atmos. Chem. Phys.*, 15(13), 7571–7583, doi:10.5194/acp-15-7571-2015, 2015.

1131 Kleipool, Q., Ludewig, A., Babić, L., Bartstra, R., Braak, R., Dierssen, W., Dewitte, P.-J., Kenter, P., Landzaat,  
 1132 R., Leloux, J., Loots, E., Meijering, P., van der Plas, E., Rozemeijer, N., Schepers, D., Schiavini, D., Smeets, J.,  
 1133 Vacanti, G., Vonk, F. and Veeffkind, P.: Pre-launch calibration results of the TROPOMI payload on-board the  
 1134 Sentinel-5 Precursor satellite, *Atmos. Meas. Tech.*, 11(12), 6439–6479, doi:10.5194/amt-11-6439-2018, 2018.

1135 Kleipool, Q. L., Dobber, M. R., de Haan, J. F. and Levelt, P. F.: Earth surface reflectance climatology from 3  
 1136 years of OMI data, *J. Geophys. Res.*, 113(D18), D18308, doi:10.1029/2008JD010290, 2008.

1137 Kluge, F., Hüneke, T., Knecht, M., Lichtenstern, M., Rotermund, M., Schlager, H., Schreiner, B. and  
 1138 Pfeilsticker, K.: Profiling of formaldehyde, glyoxal, methylglyoxal, and CO over the Amazon: Normalized  
 1139 excess mixing ratios and related emission factors in biomass burning plumes, *Atmos. Chem. Phys.*, 20(20),  
 1140 12363–12389, doi:10.5194/acp-20-12363-2020, 2020.

1141 Knote, C., Hodzic, A., Jimenez, J. L., Volkamer, R., Orlando, J. J., Baidar, S., Brioude, J., Fast, J., Gentner, D.  
 1142 R., Goldstein, A. H., Hayes, P. L., Knighton, W. B., Oetjen, H., Setyan, A., Stark, H., Thalman, R., Tyndall, G.,  
 1143 Washenfelder, R., Waxman, E. and Zhang, Q.: Simulation of semi-explicit mechanisms of SOA formation from  
 1144 glyoxal in aerosol in a 3-D model, *Atmos. Chem. Phys.*, 14, 6213–6239, doi:10.5194/acp-14-6213-2014, 2014.

1145 Kosarev, A. N., Kostianoy, A. G. and Zonn, I. S.: Kara-Bogaz-Gol bay: Physical and chemical evolution, *Aquat.*  
 1146 *Geochemistry*, 15(1–2), 223–236, doi:10.1007/s10498-008-9054-z, 2009.

1147 Kumar, V., Sarkar, C. and Sinha, V.: Influence of post-harvest crop residue fires on surface ozone mixing ratios  
 1148 in the N.W. IGP analyzed using 2years of continuous in situ trace gas measurements, *J. Geophys. Res.*, 121(7),  
 1149 3619–3633, doi:10.1002/2015JD024308, 2016.

1150 Kumar, V., Beirle, S., Dörner, S., Mishra, A. K., Donner, S., Wang, Y., Sinha, V. and Wagner, T.: Long term  
 1151 MAX-DOAS measurements of NO<sub>2</sub>, HCHO and aerosols and evaluation of corresponding satellite data  
 1152 products over Mohali in the Indo-Gangetic plain, *Atmos. Chem. Phys.*, (2), 1–62, doi:10.5194/acp-2020-404,  
 1153 2020.

1154 Lawson, S. J., Selleck, P. W., Galbally, I. E., Keywood, M. D., Harvey, M. J., Lerot, C., Helmig, D. and  
 1155 Ristovski, Z.: Seasonal in situ observations of glyoxal and methylglyoxal over the temperate oceans of the  
 1156 Southern Hemisphere, *Atmos. Chem. Phys.*, 15(1), 223–240, doi:10.5194/acp-15-223-2015, 2015.

1157 Lerot, C., Stavrakou, T., De Smedt, I., Müller, J. F., Van Roozendael, M., Müller, J. F. and Van Roozendael,  
 1158 M.: Glyoxal vertical columns from GOME-2 backscattered light measurements and comparisons with a global  
 1159 model, *Atmos. Chem. Phys.*, 10(24), 12059–12072, doi:10.5194/acp-10-12059-2010, 2010.

1160 Levelt, P. F., Van Den Oord, G. H. J., Dobber, M. R., Mälkki, A., Visser, H., De Vries, J., Stammes, P.,  
 1161 Lundell, J. O. V and Saari, H.: The Ozone Monitoring Instrument, *IEEE Trans. Geosci. Remote Sens.*, 44(5),  
 1162 1093, doi:10.1109/TGRS.2006.872333, 2006.

1163 Li, J., Mao, J., Min, K.-E., Washenfelder, R. A., Brown, S. S., Kaiser, J., Keutsch, F. N., Volkamer, R., Wolfe,  
 1164 G. M., Hanisco, T. F., Pollack, I. B., Ryerson, T. B., Graus, M., Gilman, J. B., Lerner, B. M., Warneke, C., de  
 1165 Gouw, J. A., Middlebrook, A. M., Liao, J., Welti, A., Henderson, B. H., McNeill, V. F., Hall, S. R., Ullmann,  
 1166 K., Donner, L. J., Paulot, F. and Horowitz, L. W.: Observational constraints on glyoxal production from  
 1167 isoprene oxidation and its contribution to organic aerosol over the Southeast United States, *J. Geophys. Res.*  
 1168 *Atmos.*, 121(16), 9849–9861, doi:10.1002/2016JD025331, 2016.

1169 Liu, Z., Wang, Y., Vrekoussis, M., Richter, A., Wittrock, F., Burrows, J. P., Shao, M., Chang, C.-C., Liu, S.-C.,  
 1170 Wang, H. and Chen, C.: Exploring the missing source of glyoxal (CHOCHO) over China, *Geophys. Res. Lett.*,  
 1171 39(10), L10812, doi:10.1029/2012GL051645, 2012.

1172 Lorente, A., Folkert Boersma, K., Yu, H., Dörner, S., Hilboll, A., Richter, A., Liu, M., Lamsal, L. N., Barkley,  
 1173 M., De Smedt, I., Van Roozendael, M., Wang, Y., Wagner, T., Beirle, S., Lin, J. T., Krotkov, N., Stammes, P.,  
 1174 Wang, P., Eskes, H. J. and Krol, M.: Structural uncertainty in air mass factor calculation for NO<sub>2</sub> and HCHO  
 1175 satellite retrievals, *Atmos. Meas. Tech.*, 10(3), 759–782, doi:10.5194/amt-10-759-2017, 2017.

1176 Lorente, A., Boersma, K. F., Stammes, P., Tilstra, L. G., Richter, A., Yu, H., Kharbouche, S. and Muller, J.-P.:  
 1177 The importance of surface reflectance anisotropy for cloud and NO<sub>2</sub> retrievals from GOME-2 and OMI, *Atmos.*  
 1178 *Meas. Tech.*, 11(7), 4509–4529, doi:10.5194/amt-11-4509-2018, 2018.

1179 Loyola, D. G., Xu, J., Heue, K. P. and Zimmer, W.: Applying FP-ILM to the retrieval of geometry-dependent  
 1180 effective Lambertian equivalent reflectivity (GE-LER) daily maps from UVN satellite measurements, *Atmos.*  
 1181 *Meas. Tech.*, 13(2), 985–999, doi:10.5194/amt-13-985-2020, 2020.

1182 Ludewig, A., Kleipool, Q., Bartstra, R., Landzaat, R., Leloux, J., Loots, E., Meijering, P., van der Plas, E.,  
 1183 Rozemeijer, N., Vonk, F. and Veefkind, P.: In-flight calibration results of the TROPOMI payload on board the  
 1184 Sentinel-5 Precursor satellite, *Atmos. Meas. Tech.*, 13(7), 3561–3580, doi:10.5194/amt-13-3561-2020, 2020.

1185 Lutz, R., Loyola, D., García, S. G. and Romahn, F.: OCRA radiometric cloud fractions for GOME-2 on MetOp-  
 1186 A/B, *Atmos. Meas. Tech.*, 9(5), 2357–2379, doi:10.5194/amt-9-2357-2016, 2016.

1187 Mahajan, A. S., Prados-Roman, C., Hay, T. D., Lampel, J., Pöhler, D., Großmann, K., Tschritter, J., Frieß, U.,  
 1188 Platt, U., Johnston, P., Kreher, K., Wittrock, F., Burrows, J. P., Plane, J. M. C. and Saiz-Lopez, A.: Glyoxal  
 1189 observations in the global marine boundary layer, *J. Geophys. Res. Atmos.*, n/a–n/a,

doi:10.1002/2013JD021388, 2014.

Marais, E. A., Jacob, D. J., Kurosu, T. P., Chance, K., Murphy, J. G., Reeves, C., Mills, G., Casadio, S., Millet, D. B., Barkley, M. P., Paulot, F. and Mao, J.: Isoprene emissions in Africa inferred from OMI observations of formaldehyde columns, *Atmos. Chem. Phys.*, 12(14), 6219–6235, doi:10.5194/acp-12-6219-2012, 2012.

Mason, J. D., Cone, M. T. and Fry, E. S.: Ultraviolet (250–550 nm) absorption spectrum of pure water, *Appl. Opt.*, 55(25), 7163, doi:10.1364/AO.55.007163, 2016.

Michaela Friedrich, M., Rivera, C., Stremme, W., Ojeda, Z., Arellano, J., Bezanilla, A., García-Reynoso, J. A. and Grutter, M.: NO<sub>2</sub> vertical profiles and column densities from MAX-DOAS measurements in Mexico City, *Atmos. Meas. Tech.*, 12(4), 2545–2565, doi:10.5194/amt-12-2545-2019, 2019.

Müller, J.-F. and Brasseur, G.: IMAGES: A three-dimensional chemical transport model of the global troposphere, *J. Geophys. Res.*, 100(D8), 16445, doi:10.1029/94JD03254, 1995.

Müller, J.-F., Stavrou, T., Bauwens, M., Compennolle, S. and Peeters, J.: Chemistry and deposition in the Model of Atmospheric composition at Global and Regional scales using Inversion Techniques for Trace gas Emissions (MAGRITTE v1.0). Part B. Dry deposition, *Geosci. Model Dev. Discuss.*, 1–49, doi:10.5194/gmd-2018-317, 2018.

Müller, J.-F., Stavrou, T. and Peeters, J.: Chemistry and deposition in the Model of Atmospheric composition at Global and Regional scales using Inversion Techniques for Trace gas Emissions (MAGRITTE v1.1) – Part 1: Chemical mechanism, *Geosci. Model Dev.*, 12(6), 2307–2356, doi:10.5194/gmd-12-2307-2019, 2019.

Müller, J. F., Stavrou, T., Wallens, S., De Smedt, I., Van Roozendaal, M., Potosnak, M. J., Rinne, J., Munger, B., Goldstein, A. and Guenther, A. B.: Global isoprene emissions estimated using MEGAN, ECMWF analyses and a detailed canopy environment model, *Atmos. Chem. Phys.*, 8(5), 1329–1341, doi:10.5194/acp-8-1329-2008, 2008.

Munro, R., Lang, R., Klaes, D., Poli, G., Retscher, C., Lindstrot, R., Huckle, R., Lacan, A., Grzegorski, M., Holdak, A., Kokhanovsky, A., Livschitz, J. and Eisinger, M.: The GOME-2 instrument on the Metop series of satellites: instrument design, calibration, and level 1 data processing – an overview, *Atmos. Meas. Tech.*, 9(3), 1279–1301, doi:10.5194/amt-9-1279-2016, 2016.

Myriokefalitakis, S., Vrekoussis, M., Tsigaridis, K., Wittrock, F., Richter, A., Brühl, C., Volkamer, R., Burrows, J. P. and Kanakidou, M.: The influence of natural and anthropogenic secondary sources on the glyoxal global distribution, *Atmos. Chem. Phys.*, 8(16), 4965–4981 [online] Available from: <http://www.atmos-chem-phys.net/8/4965/2008/>, 2008.

Noël, S., Bramstedt, K., Bovensmann, H., Gerilowski, K., Burrows, J. P., Standfuss, C., Dufour, E. and Veihelmann, B.: Quantification and mitigation of the impact of scene inhomogeneity on Sentinel-4 UVN UV-VIS retrievals, *Atmos. Meas. Tech.*, 5(6), 1319–1331, doi:10.5194/amt-5-1319-2012, 2012.

Palmer, P. I., Jacob, D. J., Chance, K., Martin, R. V., Spurr, R. J. D., Kurosu, T. P., Bey, I., Yantosca, R., Fiore, A. and Li, Q.: Air mass factor formulation for spectroscopic measurements from satellites: Application to

1225 formaldehyde retrievals from the Global Ozone Monitoring Experiment, *J. Geophys. Res. Atmos.*, 106(D13),  
1226 14539–14550, doi:10.1029/2000JD900772, 2001.

1227 Palmer, P. I., Abbot, D. S., Fu, T.-M., Jacob, D. J., Chance, K., Kurosu, T. P., Guenther, A., Wiedinmyer, C.,  
1228 Stanton, J. C., Pilling, M. J., Pressley, S. N., Lamb, B. and Sumner, A. L.: Quantifying the seasonal and  
1229 interannual variability of North American isoprene emissions using satellite observations of the formaldehyde  
1230 column, *J. Geophys. Res.*, 111(D12), D12315, doi:10.1029/2005JD006689, 2006.

1231 Peters, E., Wittrock, F., Richter, A., Alvarado, L. M. A., Rozanov, V. V. and Burrows, J. P.: Liquid water  
1232 absorption and scattering effects in DOAS retrievals over oceans, *Atmos. Meas. Tech.*, 7(12), 4203–4221,  
1233 doi:10.5194/amt-7-4203-2014, 2014.

1234 Platt, U. and Stutz, J.: *Differential Optical Absorption Spectroscopy: Principles and Applications*, Springer-  
1235 Verlag., 2008.

1236 Puķīte, J., Köhl, S., Deutschmann, T., Platt, U. and Wagner, T.: Extending differential optical absorption  
1237 spectroscopy for limb measurements in the UV, *Atmos. Meas. Tech.*, 3(3), 631–653, doi:10.5194/amt-3-631-  
1238 2010, 2010.

1239 Richter, A.: qa4ecv\_no2\_inhomogeneous\_scenes\_171221, in QA4ECV technical note, Treatment of  
1240 inhomogeneous scenes., 2018.

1241 Richter, A. and Burrows, J. P.: Tropospheric NO<sub>2</sub> from GOME measurements, *Adv. Sp. Res.*, 29(11), 1673–  
1242 1683, doi:10.1016/S0273-1177(02)00100-X, 2002.

1243 Richter, A., Begoin, M., Hilboll, A. and Burrows, J. P.: An improved NO<sub>2</sub> retrieval for  
1244 the GOME-2 satellite instrument, *Atmos. Meas. Tech.*, 4(6), 1147–1159, doi:10.5194/amt-4-1147-2011, 2011.

1245 Richter, A., Hilboll, A., Sanders, A., Peters, E. and Burrows, J. P.: Inhomogeneous scene effects in OMI NO<sub>2</sub>  
1246 observations, EGU General Assembly 2018. [online] Available from: [http://www.doas-](http://www.doas-bremen.de/posters/egu_2018_richter.pdf)  
1247 [bremen.de/posters/egu\\_2018\\_richter.pdf](http://www.doas-bremen.de/posters/egu_2018_richter.pdf) (Accessed 19 May 2021), 2018.

1248 Rothman, L. S., Gordon, I. E., Babikov, Y., Barbe, A., Chris Benner, D., Bernath, P. F., Birk, M., Bizzocchi, L.,  
1249 Boudon, V., Brown, L. R., Campargue, A., Chance, K., Cohen, E. A., Coudert, L. H., Devi, V. M., Drouin, B.  
1250 J., Fayt, A., Flaud, J. M., Gamache, R. R., Harrison, J. J., Hartmann, J. M., Hill, C., Hodges, J. T., Jacquemart,  
1251 D., Jolly, A., Lamouroux, J., Le Roy, R. J., Li, G., Long, D. A., Lyulin, O. M., Mackie, C. J., Massie, S. T.,  
1252 Mikhailenko, S., Müller, H. S. P., Naumenko, O. V., Nikitin, A. V., Orphal, J., Perevalov, V., Perrin, A.,  
1253 Polovtseva, E. R., Richard, C., Smith, M. A. H., Starikova, E., Sung, K., Tashkun, S., Tennyson, J., Toon, G. C.,  
1254 Tyuterev, V. G. and Wagner, G.: The HITRAN2012 molecular spectroscopic database, *J. Quant. Spectrosc.*  
1255 *Radiat. Transf.*, 130, 4–50, doi:10.1016/j.jqsrt.2013.07.002, 2013.

1256 Rozanov, A., Rozanov, V., Buchwitz, M., Kokhanovsky, A. and Burrows, J. P.: SCIATRAN 2.0 - A new  
1257 radiative transfer model for geophysical applications in the 175-2400 nm spectral region, in *Advances in Space*  
1258 *Research*, vol. 36, pp. 1015–1019, Elsevier Ltd., 2005.

1259 Schenkeveld, V. M. E., Jaross, G., Marchenko, S., Haffner, D., Kleipool, Q. L., Rozemeijer, N. C., Pepijn



1260 Veefkind, J. and Levelt, P. F.: In-flight performance of the Ozone Monitoring Instrument, *Atmos. Meas. Tech.*,  
1261 10, doi:10.5194/amt-10-1957-2017, 2017.

1262 Schreier, S. F., Richter, A., Peters, E., Ostendorf, M., Schmalwieser, A. W., Weihs, P. and Burrows, J. P.: Dual  
1263 ground-based MAX-DOAS observations in Vienna, Austria: Evaluation of horizontal and temporal NO<sub>2</sub>,  
1264 HCHO, and CHOCHO distributions and comparison with independent data sets, *Atmos. Environ.* X, 5, 100059,  
1265 doi:10.1016/J.AEAOA.2019.100059, 2020.

1266 Serdyuchenko, A., Gorshelev, V., Weber, M., Chehade, W. and Burrows, J. P.: High spectral resolution ozone  
1267 absorption cross-sections &ndash; Part 2: Temperature dependence, *Atmos. Meas. Tech.*, 7(2), 625–636,  
1268 doi:10.5194/amt-7-625-2014, 2014.

1269 Sinreich, R., Coburn, S., Dix, B. and Volkamer, R.: Ship-based detection of glyoxal over the remote tropical  
1270 Pacific Ocean, *Atmos. Chem. Phys.*, 10(23), 11359–11371, doi:10.5194/acp-10-11359-2010, 2010.

1271 Stavrakou, T., Müller, J.-F., De Smedt, I., Van Roozendaal, M., Van Der Werf, G. R., Giglio, L. and Guenther,  
1272 A.: Evaluating the performance of pyrogenic and biogenic emission inventories against one decade of space-  
1273 based formaldehyde columns. [online] Available from: [www.atmos-chem-phys.net/9/1037/2009/](http://www.atmos-chem-phys.net/9/1037/2009/) (Accessed 19  
1274 March 2021a), 2009.

1275 Stavrakou, T., Müller, J.-F., De Smedt, I., Van Roozendaal, M., Kanakidou, M., Vrekoussis, M., Wittrock, F.,  
1276 Richter, A. and Burrows, J. P.: The continental source of glyoxal estimated by the synergistic use of spaceborne  
1277 measurements and inverse modelling, *Atmos. Chem. Phys.*, 9(21), 8431–8446 [online] Available from:  
1278 <http://www.atmos-chem-phys.net/9/8431/2009/>, 2009b.

1279 Stavrakou, T., Müller, J.-F., Boersma, K. F., van der A, R. J., Kurokawa, J., Ohara, T. and Zhang, Q.: Key  
1280 chemical NO<sub>x</sub> sink uncertainties and how they influence top-down emissions of nitrogen oxides, *Atmos. Chem.*  
1281 *Phys.*, 13(17), 9057–9082, doi:10.5194/acp-13-9057-2013, 2013.

1282 Stavrakou, T., Müller, J.-F., Bauwens, M., Smedt, I. De, Lerot, C., Roozendaal, M. Van, Coheur, P.-F.,  
1283 Clerbaux, C., Boersma, K. F., A, R. van der, Song, Y., Jeong, S.-J., Huang, X., Song, Y., Li, M., Li, J., Zhu, T.,  
1284 Yamaji, K., Werf, G. R. van der, Huang, X., Li, M., Li, J., Song, Y., Fu, T.-M., Levelt, P. F., Smedt, I. De,  
1285 Smedt, I. De, Boersma, K. F., Lerot, C., Müller, J.-F., Stavrakou, T., Stavrakou, T., Müller, J.-F., Smedt, I. De,  
1286 Roozendaal, M. Van, Werf, G. van der, Giglio, L., Guenther, A., Stavrakou, T., Guenther, A., Karl, T., Harley,  
1287 P., Wiedinmyer, C., Palmer, P. I., Geron, C., Li, M., Andreae, M. O., Merlet, P., Akagi, S., Kurokawa, J., Sun,  
1288 L., Jin, X., Holloway, T., Safieddine, S., Chaudhry, Z., Shi, Z., Tao, J. Z., Wang, Z., Han, D., Li, S., Su, L.,  
1289 Chen, L., Deng, X., Dee, D. P., Randerson, J., Chen, Y., Werf, G., Rogers, B., Morton, D., Kaiser, J.,  
1290 Wiedinmyer, C., Kudo, S., Inomata, S., Warneke, C., Yokelson, R. J., Korontzi, S., McCarty, J., Loboda, T.,  
1291 Kumar, S., Justice, C., Fu, T.-M., Stavrakou, T., Castellanos, P., Boersma, K. F., Werf, G. R. van der, Razavi,  
1292 A., Stavrakou, T., Lin, J., Castellanos, P., Boersma, K. F., Torres, O., Haan, J. F. de, Barkley, M. P., Roberts,  
1293 G., Wooster, M. J., Lagoudakis, E., Stavrakou, T., Miller, C. C., Jacob, D. J., et al.: Substantial Underestimation  
1294 of Post-Harvest Burning Emissions in the North China Plain Revealed by Multi-Species Space Observations,  
1295 *Sci. Reports*, Publ. online 31 August 2016; | doi10.1038/srep32307, 6, 615–619, doi:10.1038/SREP32307, 2016.

1296 Thalman, R. and Volkamer, R.: Temperature dependent absorption cross-sections of O<sub>2</sub>–O<sub>2</sub> collision pairs

1297 between 340 and 630 nm and at atmospherically relevant pressure, *Phys. Chem. Chem. Phys.*, 15(37), 15371,  
1298 doi:10.1039/c3cp50968k, 2013.

1299 Theys, N., Volkamer, R., Müller, J. F., Zarzana, K. J., Kille, N., Clarisse, L., De Smedt, I., Lerot, C.,  
1300 Finkenzeller, H., Hendrick, F., Koenig, T. K., Lee, C. F., Knote, C., Yu, H. and Van Roozendaal, M.: Global  
1301 nitrous acid emissions and levels of regional oxidants enhanced by wildfires, *Nat. Geosci.*, 13(10), 681–686,  
1302 doi:10.1038/s41561-020-0637-7, 2020.

1303 Tilstra, L., Tuinder, O., Wang, P. and Stammes, P.: Directionally dependent Lambertian-equivalent reflectivity  
1304 (DLER) of the Earth’s surface measured by the GOME-2 satellite instruments, *Atmos. Meas. Tech. Discuss.*, 1–  
1305 29, doi:10.5194/amt-2020-502, 2021.

1306 Tilstra, L. G., Tuinder, O. N. E., Wang, P. and Stammes, P.: Surface reflectivity climatologies from UV to NIR  
1307 determined from Earth observations by GOME-2 and SCIAMACHY, *J. Geophys. Res. Atmos.*,  
1308 doi:10.1002/2016JD025940, 2017.

1309 Torres, O., Bhartia, P. K., Jethva, H. and Ahn, C.: Impact of the ozone monitoring instrument row anomaly on  
1310 the long-term record of aerosol products, *Atmos. Meas. Tech.*, 11, 2701–2715, doi:10.5194/amt-11-2701-2018,  
1311 2018.

1312 Valks, P., Hao, N. and Lerot, C.: Algorithm Theoretical Basis Document for GOME-2 glyoxal column data  
1313 records, SAF/AC/DLR/ATBD/GLY/01; Iss. 1/B., 2020.

1314 Vandaele, A. C., Hermans, C., Simon, P. C., Carleer, M., Colin, R., Fally, S., Mérienne, M. F., Jenouvrier, A.  
1315 and Coquart, B.: Measurements of the NO<sub>2</sub> absorption cross-section from 42 000 cm<sup>-1</sup> to 10 000 cm<sup>-1</sup> (238–  
1316 1000 nm) at 220 K and 294 K, *J. Quant. Spectrosc. Radiat. Transf.*, 59(3–5), 171–184, doi:10.1016/S0022-  
1317 4073(97)00168-4, 1998.

1318 Veefkind, J. P., Aben, I., McMullan, K., Förster, H., de Vries, J., Otter, G., Claas, J., Eskes, H. J., de Haan, J. F.,  
1319 Kleipool, Q., van Weele, M., Hasekamp, O., Hoogeveen, R., Landgraf, J., Snel, R., Tol, P., Ingmann, P., Voors,  
1320 R., Kruizinga, B., Vink, R., Visser, H. and Levelt, P. F.: TROPOMI on the ESA Sentinel-5 Precursor: A GMES  
1321 mission for global observations of the atmospheric composition for climate, air quality and ozone layer  
1322 applications, *Remote Sens. Environ.*, 120, 70–83, doi:10.1016/j.rse.2011.09.027, 2012.

1323 Veefkind, J. P., Haan, J. F. de, Sneep, M. and Levelt, P. F.: Improvements to the OMI O<sub>2</sub>–O<sub>2</sub> operational cloud  
1324 algorithm and comparisons with ground-based radar–lidar observations, *Atmos. Meas. Tech.*, 9(12), 6035–6049,  
1325 doi:10.5194/AMT-9-6035-2016, 2016.

1326 Verhoelst, T., Compernelle, S., Pinardi, G., Lambert, J. C., Eskes, H. J., Eichmann, K. U., Fjæraa, A. M.,  
1327 Granville, J., Niemeijer, S., Cede, A., Tiefengraber, M., Hendrick, F., Pazmiño, A., Bais, A., Bazureau, A.,  
1328 Folkert Boersma, K., Bogner, K., Dehn, A., Donner, S., Elokhov, A., Gebetsberger, M., Goutail, F., Grutter De  
1329 La Mora, M., Gruzdev, A., Gratsea, M., Hansen, G. H., Irie, H., Jepsen, N., Kanaya, Y., Karagiozidis, D., Kivi,  
1330 R., Kreher, K., Levelt, P. F., Liu, C., Müller, M., Navarro Comas, M., Piders, A. J. M., Pommereau, J. P.,  
1331 Portafaix, T., Prados-Roman, C., Puentedura, O., Querel, R., Remmers, J., Richter, A., Rimmer, J., Cárdenas, C.  
1332 R., De Miguel, L. S., Sinyakov, V. P., Stremme, W., Strong, K., Van Roozendaal, M., Pepijn Veefkind, J.,

1333 Wagner, T., Wittrock, F., Yela González, M. and Zehner, C.: Ground-based validation of the Copernicus  
 1334 Sentinel-5P TROPOMI NO<sub>2</sub> measurements with the NDACC ZSL-DOAS, MAX-DOAS and Pandonia global  
 1335 networks, *Atmos. Meas. Tech.*, 14(1), 481–510, doi:10.5194/amt-14-481-2021, 2021.

1336 Vigouroux, C., Langerock, B., Bauer Aquino, C. A., Blumenstock, T., Cheng, Z., De Mazière, M., De Smedt, I.,  
 1337 Grutter, M., Hannigan, J. W., Jones, N., Kivi, R., Loyola, D., Lutsch, E., Mahieu, E., Makarova, M., Metzger,  
 1338 J.-M., Morino, I., Murata, I., Nagahama, T., Notholt, J., Ortega, I., Palm, M., Pinardi, G., Röhling, A., Smale,  
 1339 D., Stremme, W., Strong, K., Sussmann, R., Té, Y., van Roozendaal, M., Wang, P. and Winkler, H.:  
 1340 TROPOMI–Sentinel-5 Precursor formaldehyde validation using an extensive network of ground-based Fourier-  
 1341 transform infrared stations, *Atmos. Meas. Tech.*, 13(7), 3751–3767, doi:10.5194/amt-13-3751-2020, 2020.

1342 Vohra, K., Vodonos, A., Schwartz, J., Marais, E. A., Sulprizio, M. P. and Mickley, L. J.: Global mortality from  
 1343 outdoor fine particle pollution generated by fossil fuel combustion: Results from GEOS-Chem, *Environ. Res.*,  
 1344 195, 110754, doi:10.1016/j.envres.2021.110754, 2021.

1345 Volkamer, R., Spietz, P., Burrows, J. and Platt, U.: High-resolution absorption cross-section of glyoxal in the  
 1346 UV—vis and IR spectral ranges, *J. Photochem. Photobiol. A Chem.*, 172(1), 35—46 [online] Available from:  
 1347 [http://www.colorado.edu/chemistry/volkamer/publications/articles/Volkamer et al \(2005\) HR cross section](http://www.colorado.edu/chemistry/volkamer/publications/articles/Volkamer%20et%20al%20(2005)%20HR%20cross%20section%20glyoxal.pdf)  
 1348 [glyoxal.pdf](http://www.colorado.edu/chemistry/volkamer/publications/articles/Volkamer et al (2005) HR cross section glyoxal.pdf), 2005.

1349 Volkamer, R., San Martini, F., Molina, L. T., Salcedo, D., Jimenez, J. L. and Molina, M. J.: A missing sink for  
 1350 gas-phase glyoxal in Mexico City: Formation of secondary organic aerosol, *Geophys. Res. Lett.*, 34(19),  
 1351 L19807, doi:10.1029/2007GL030752, 2007.

1352 Volkamer, R., Baidar, S., Campos, T. L., Coburn, S., DiGangi, J. P., Dix, B., Eloranta, E. W., Koenig, T. K.,  
 1353 Morley, B., Ortega, I., Pierce, B. R., Reeves, M., Sinreich, R., Wang, S., Zondlo, M. A. and Romashkin, P. A.:  
 1354 Aircraft measurements of BrO, IO, glyoxal, NO<sub>2</sub>, H<sub>2</sub>O, O<sub>2</sub>–O<sub>2</sub> and aerosol extinction profiles in the tropics:  
 1355 comparison with aircraft-/ship-based in situ and lidar measurements, *Atmos. Meas. Tech.*, 8(5), 2121–2148,  
 1356 doi:10.5194/amt-8-2121-2015, 2015.

1357 Voors, R., Dobber, M., Dirksen, R. and Levelt, P.: Method of calibration to correct for cloud-induced  
 1358 wavelength shifts in the Aura satellite’s Ozone Monitoring Instrument, *Appl. Opt.*, 45(15), 3652–3658,  
 1359 doi:10.1364/AO.45.003652, 2006.

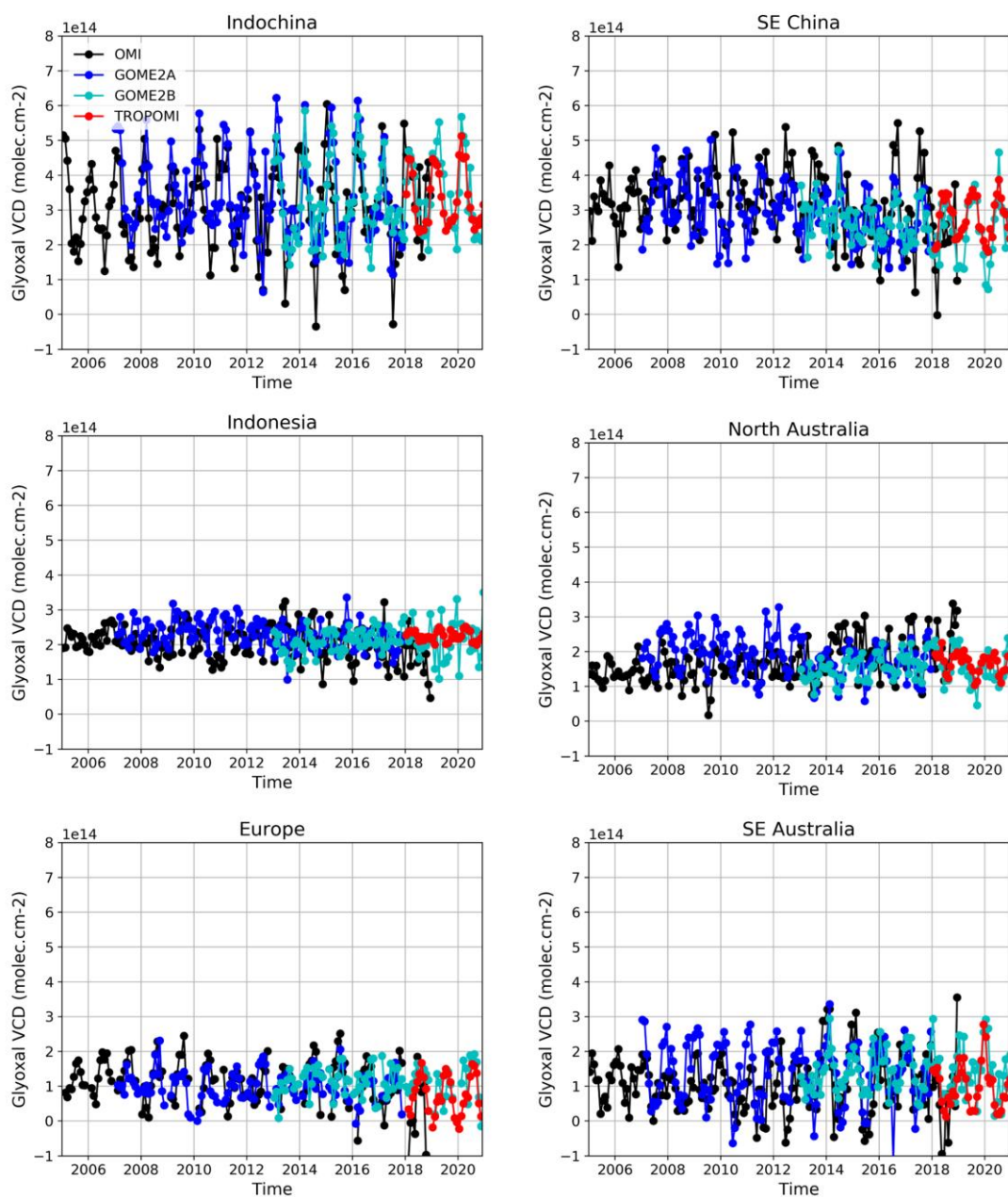
1360 Vrekoussis, M., Wittrock, F., Richter, A. and Burrows, J. P.: Temporal and spatial variability of glyoxal as  
 1361 observed from space, *Atmos. Chem. Phys.*, 9(13), 4485–4504, doi:10.5194/acp-9-4485-2009, 2009.

1362 Vrekoussis, M., Wittrock, F., Richter, A. and Burrows, J. P.: GOME-2 observations of oxygenated VOCs: what  
 1363 can we learn from the ratio glyoxal to formaldehyde on a global scale?, *Atmos. Chem. Phys.*, 10(21), 10145–  
 1364 10160, doi:10.5194/acp-10-10145-2010, 2010.

1365 Wagner, T., Beirle, S. and Deutschmann, T.: Three-dimensional simulation of the Ring effect in observations of  
 1366 scattered sun light using Monte Carlo radiative transfer models, *Atmos. Meas. Tech.*, 2(1), 113–124,  
 1367 doi:10.5194/amt-2-113-2009, 2009.

1368 Wells, K. C., Millet, D. B., Payne, V. H., Deventer, M. J., Bates, K. H., de Gouw, J. A., Graus, M., Warneke, C.,

- Wisthaler, A. and Fuentes, J. D.: Satellite isoprene retrievals constrain emissions and atmospheric oxidation, *Nature*, 585(7824), 225–233, doi:10.1038/s41586-020-2664-3, 2020.
- Van Der Werf, G. R., Randerson, J. T., Giglio, L., Van Leeuwen, T. T., Chen, Y., Rogers, B. M., Mu, M., Van Marle, M. J. E., Morton, D. C., Collatz, G. J., Yokelson, R. J. and Kasibhatla, P. S.: Global fire emissions estimates during 1997–2016, *Earth Syst. Sci. Data*, 9(2), 697–720, doi:10.5194/essd-9-697-2017, 2017.
- Wittrock, F., Richter, A., Oetjen, H., Burrows, J. P., Kanakidou, M., Myriokefalitakis, S., Volkamer, R., Beirle, S., Platt, U. and Wagner, T.: Simultaneous global observations of glyoxal and formaldehyde from space, *Geophys. Res. Lett.*, 33(16), L16804, doi:10.1029/2006GL026310, 2006.
- World Health Organization: Ambient air pollution: A global assessment of exposure and burden of disease. [online] Available from: <https://apps.who.int/iris/handle/10665/250141> (Accessed 19 March 2021), 2016.
- Zara, M., Boersma, K. F., De Smedt, I., Richter, A., Peters, E., Van Geffen, J. H. G. M., Beirle, S., Wagner, T., Van Roozendaal, M., Marchenko, S., Lamsal, L. N. and Eskes, H. J.: Improved slant column density retrieval of nitrogen dioxide and formaldehyde for OMI and GOME-2A from QA4ECV: intercomparison, uncertainty characterization, and trends, *Atmos. Meas. Tech. Discuss.*, 11(7), 1–47, doi:10.5194/amt-11-4033-2018, 2018.
- Zhou, Y., Brunner, D., Boersma, K. F., Dirksen, R. and Wang, P.: An improved tropospheric NO<sub>2</sub> retrieval for OMI observations in the vicinity of mountainous terrain, *Atmos. Meas. Tech.*, 2(2), 401–416, doi:10.5194/amt-2-401-2009, 2009.



1401  
 1402 **Figure S1: Comparison of the monthly median glyoxal VCD time series from GOME-2A/B, OMI and TROPOMI in a**  
 1403 **few selected regions worldwide.**

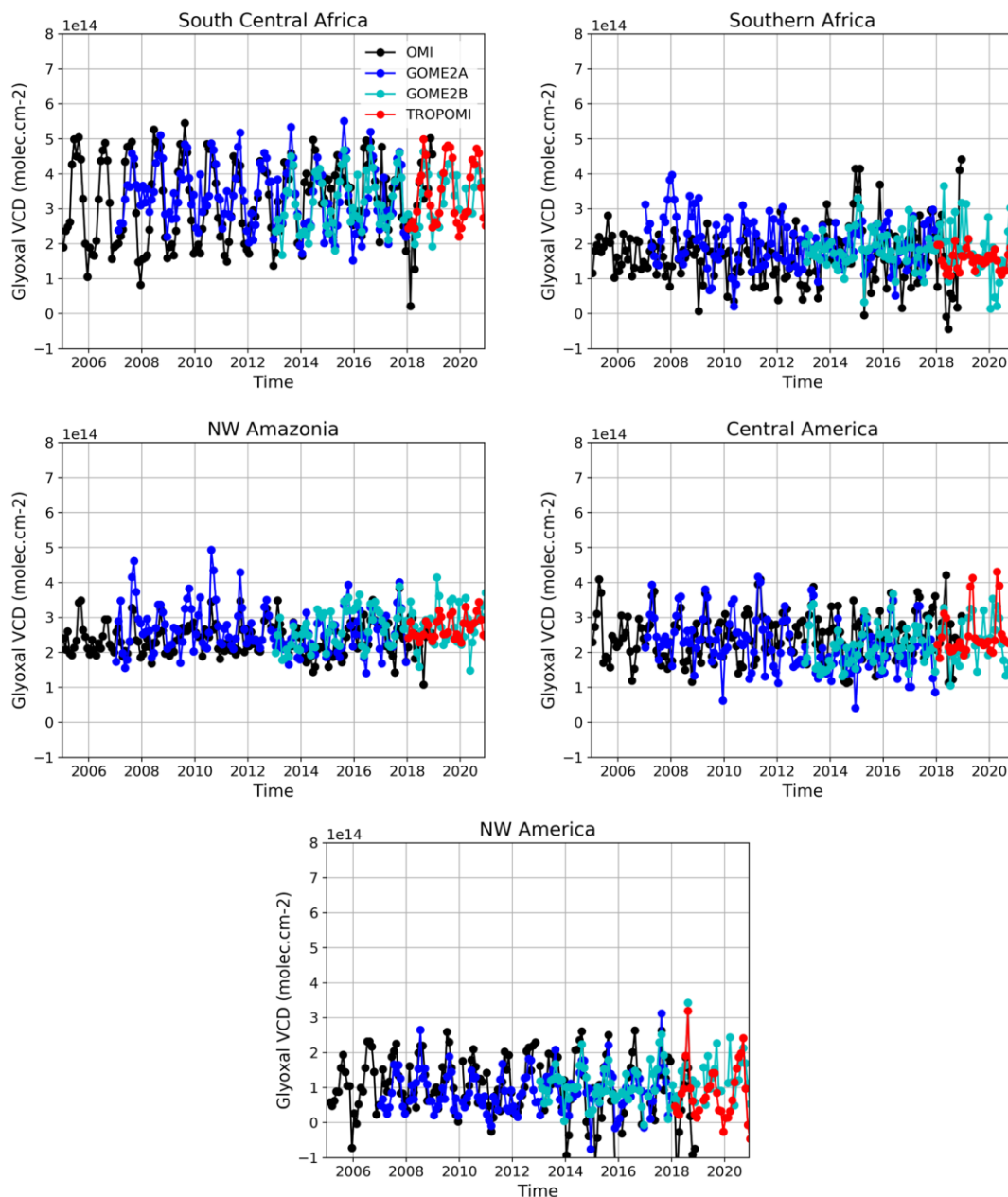


**Figure S2: Comparison of the monthly median glyoxal VCD time series from GOME-2A/B, OMI and TROPOMI in a few selected regions worldwide.**



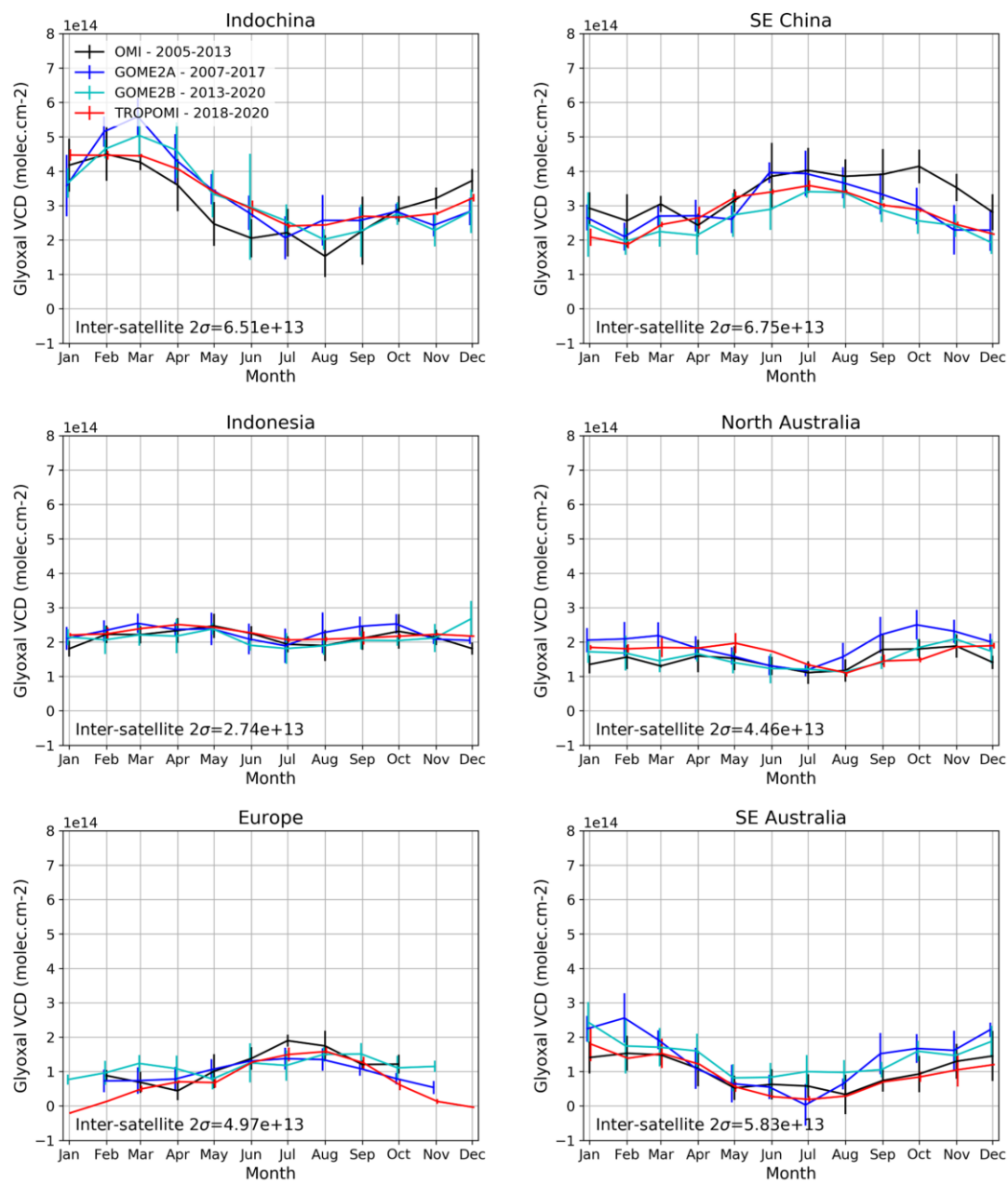


**Figure S3: Comparison of the climatological seasonal variation of the monthly median glyoxal VCDs from GOME-2A/B, OMI and TROPOMI in a few selected regions worldwide. The error bars represent the interannual variability as derived from the full time series.**

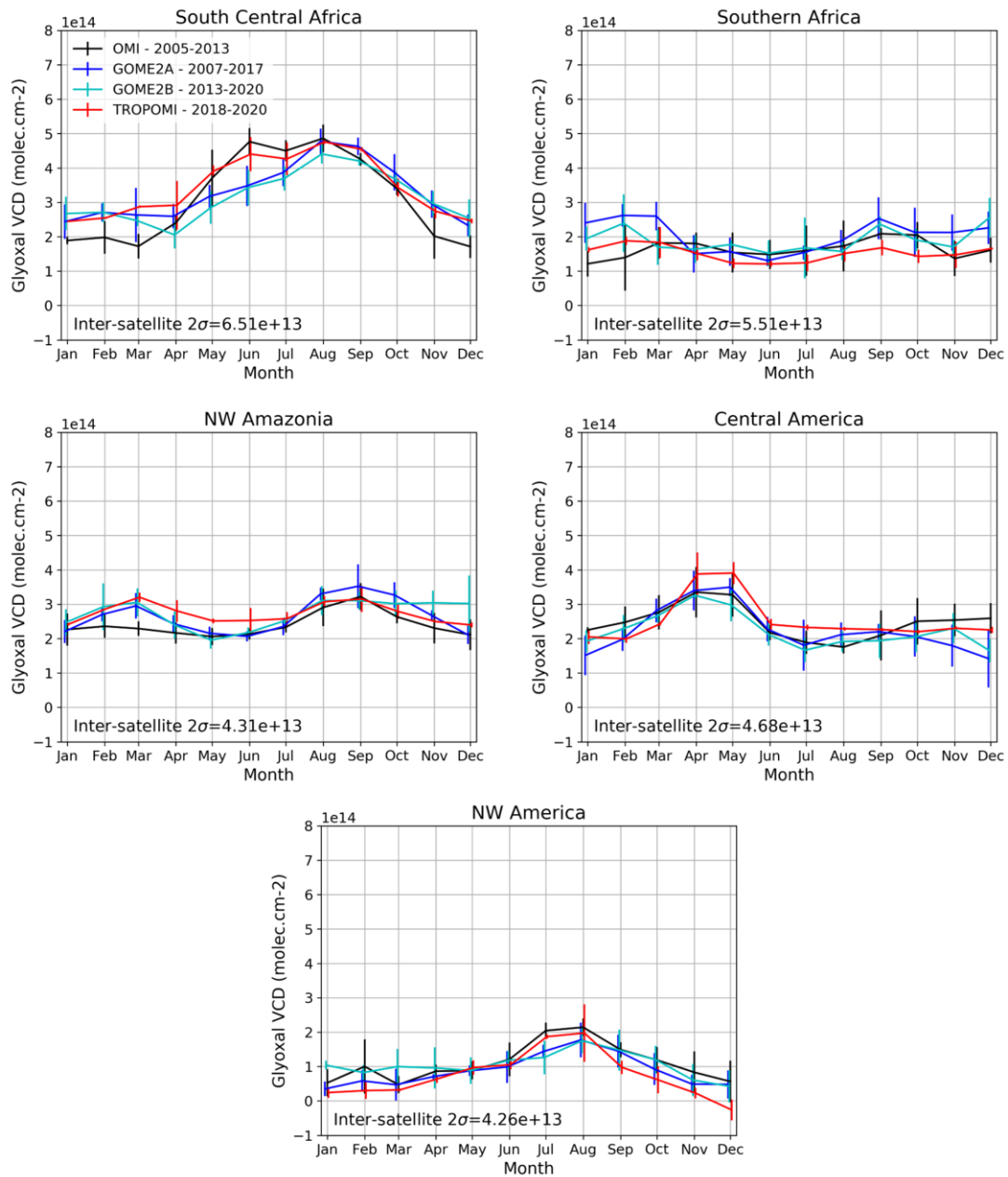


**Figure S4: Comparison of the climatological seasonal variation of the monthly median glyoxal VCDs from GOME-2A/B, OMI and TROPOMI in a few selected regions worldwide. The error bars represent the interannual variability as derived from the full time series.**